

---

# Faithful Embeddings of Irregular and Asynchronous Data for Online Log-NCDEs

---

**Benjamin Walker**  
Mathematical Institute  
University of Oxford

**Alexandre Bloch**  
Mathematical Institute  
University of Oxford

**Lingyi Yang**  
School of Mathematical Sciences  
University of Nottingham

**Sam Morley**  
Mathematical Institute  
University of Oxford

**Terry Lyons**  
Mathematical Institute, University of Oxford  
Department of Mathematics, Imperial College London

## Abstract

Continuous-time models are a natural choice for irregular and asynchronous data. A central design choice is how to embed discrete observations into continuous time. Interpolation- and imputation-based embeddings reconstruct a continuous observation path, making the model sensitive to the choice of reconstruction. We show that this reconstruction step is unnecessary; under mild conditions, compact-set universality on the model input space transfers to the data space whenever the embedding from data to input is continuous and injective. Guided by this result, and building on the rectilinear control path for Neural Controlled Differential Equations (NCDEs), we introduce a continuous and injective embedding for Log-NCDEs, a universal class of continuous-time models. Our approach records observations as increments and composes them over arbitrary query intervals to directly form log-signatures. This provides interval-level summaries without first interpolating the observed variables, while supporting online computation. Experiments on synthetic controlled dynamics and real-world time-series datasets show that the representation is accurate, efficient, and robust to irregular, asynchronous, and sparse observations.

## 1 Introduction

Sequence architectures, such as Transformers [Vaswani et al., 2017], Structured State-Space Models (SSMs) [Gu et al., 2022, Gu and Dao, 2024], and Recurrent Neural Networks (RNNs), are built around discrete updates on a prescribed grid [Elman, 1990, Hochreiter and Schmidhuber, 1997]. This discretisation is natural for text and regularly sampled time series, but is limiting in interactive and physical settings, where observations arrive irregularly, actions are taken asynchronously, and the underlying environment continues to evolve between measurements [Marvasti, 2001, Heemels et al., 2012]. Continuous-time machine learning provides a natural framework for such data [Pearlmutter, 1989, Rico-Martínez et al., 1992]. Given a continuous-time embedding of the observations, the hidden state can evolve continuously and be queried at arbitrary times [Kidger et al., 2020].

A central design choice is how to construct this embedding. One common strategy is to complete the data by imputation, interpolation, or learned interpolation before applying a model [Che et al., 2018, Shukla and Marlin, 2019, 2021, Challu et al., 2023, Wang et al., 2025]. Neural Controlled Differential Equations (NCDEs) and ContiFormer are prominent examples of this approach [Kidger et al., 2020, Morrill et al., 2022, Jhin et al., 2022, Chen et al., 2023]. Other models avoid explicit interpolation by combining continuous latent dynamics with discrete updates, as in ODE-RNNs and

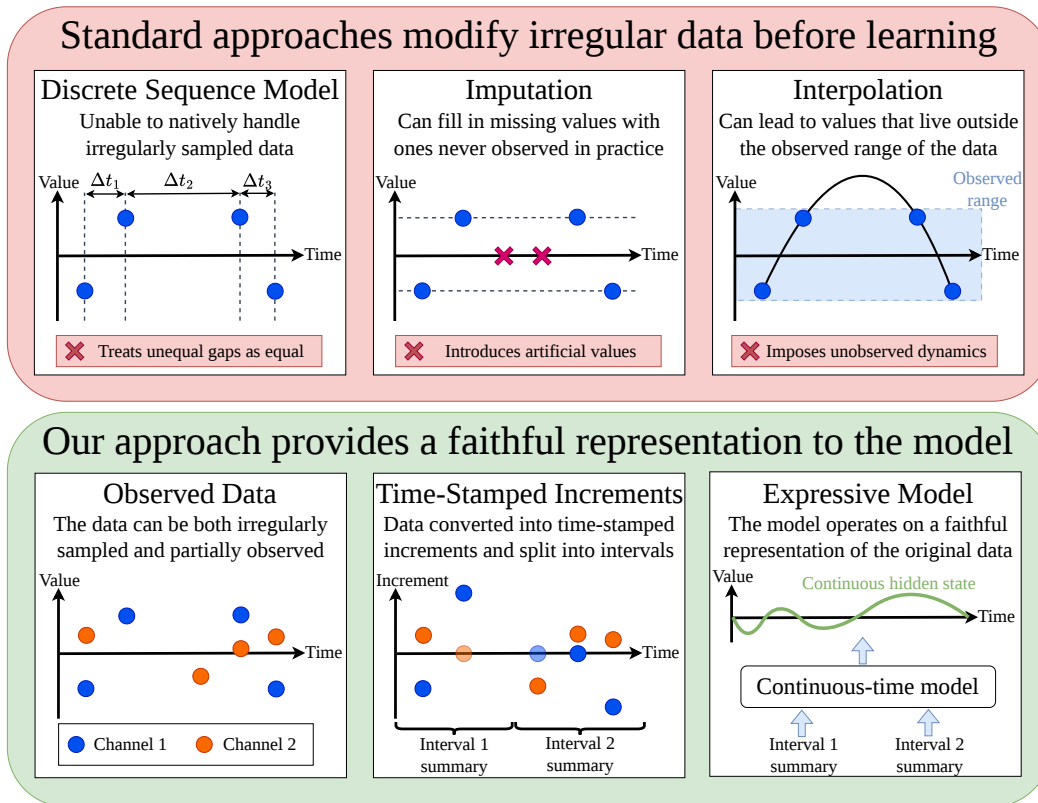


Figure 1: **Faithful representations of irregular data.** Imputation and interpolation complete the data before modelling, introducing values or dynamics that may be unrealistic. Our approach records the observed stream as time-stamped increments and groups them into interval summaries, giving a faithful (continuous and injective) representation of the discrete and irregular data.

GRU-ODE-Bayes [Rubanova et al., 2019, De Brouwer et al., 2019]. These approaches differ in how they represent discrete, irregular, and asynchronous data in continuous time.

The central principle of this paper is that a continuous-time representation of discrete observations should preserve only the information that was observed, rather than guess the unobserved behaviour between measurements. The latter should form part of the modelling as opposed to part of the representation. When guesses are built into the representation, the model may consume unrealistic inputs, as illustrated in Figure 1. Morrill et al. [2022] studied control-path embeddings for NCDEs, exploring properties such as online, smooth, bounded, and unique, or equivalently injective. For Log-NCDEs, smoothness is no longer intrinsic, since the model uses log-signatures on intervals rather than pointwise values of a control path [Walker et al., 2024]. We prove that, when the data and model input spaces are Hausdorff, universality of the model on compact subsets of its input space transfers to the data space as long as the data embedding is continuous and injective. We call such embeddings *faithful*. Since NCDEs and Log-NCDEs are universal on path space [Kidger et al., 2020, Walker et al., 2024], this result applies to both model classes for faithful observation embeddings.

This leads to three desiderata for a Log-NCDE control-path embedding. It should be faithful, computable online, and support efficient calculation of the embedded path’s log-signature over arbitrary query intervals. We construct such an embedding by mapping each observation to a local log-signature contribution that records which channels were observed and their values. These contributions compose over arbitrary query intervals, so the representation can be built directly from the observations in each interval. Continuously observed variables, such as time, contribute between observations. Figure 1 illustrates our approach.

This yields a faithful representation of the observed stream without interpolation, decouples the input sampling times from the output grid, and supports parallel-in-time computation. The resulting

algebraic formulation can also accommodate observations beyond first-order channel values, such as the signed area. In the first-order case with time as the only continuously observed variable, the continuous path corresponding to our embedding is the rectilinear control path introduced for NCDEs by Morrill et al. [2022]. Our construction can therefore be viewed as a Log-NCDE-compatible generalisation of the rectilinear scheme.

Our contributions are as follows:

- We formalise the notion of a faithful embedding and prove that faithful embeddings transfer universality from compact subsets of one Hausdorff space to another in Section 2.1.
- We introduce a faithful control-path embedding for Log-NCDEs whose interval log-signatures can be computed efficiently over arbitrary intervals in Section 2.4.
- We demonstrate the computational benefits and robustness to irregularity of the resulting models on synthetic controlled systems and real-world time-series classification in Section 3.

## 2 Faithful Embeddings of Irregular Time Series for Log-NCDEs

### 2.1 Faithful Embeddings

Before modelling, data must be embedded into the model input space. We call such an embedding *faithful* if it is continuous and injective, thus ensuring that nearby data remain nearby after embedding and that distinct data remain distinguishable. Together, these conditions are sufficient for universality to transfer from the downstream model to the original data space, as formalised by the following lemma.

**Lemma 1** (Universality Transfer). *Let  $\mathcal{X}$  and  $\mathcal{P}$  be Hausdorff topological spaces, and let  $\varphi : \mathcal{X} \rightarrow \mathcal{P}$  be a continuous injection. Suppose  $\mathcal{F} \subseteq C(\mathcal{P}; \mathbb{R})$  is a family of continuous real-valued functions such that for every compact  $K \subseteq \mathcal{P}$ , the restrictions  $\mathcal{F}|_K$  are dense in  $C(K; \mathbb{R})$  in the uniform topology. Then for every compact  $K_0 \subseteq \mathcal{X}$ , the restrictions  $(\mathcal{F} \circ \varphi)|_{K_0}$  are dense in  $C(K_0; \mathbb{R})$  in the uniform topology, where  $\mathcal{F} \circ \varphi := \{f \circ \varphi : f \in \mathcal{F}\}$ .*

The proof is in Appendix A. With  $\mathcal{X}$  the data space,  $\mathcal{P}$  the model input space, and  $\varphi$  the embedding, Lemma 1 shows that faithful embeddings transfer universality back to the original data. This recovers the usual signature-universality argument: Stone–Weierstrass gives universality on signature space, and injectivity transfers it back to paths [Stone, 1948, Levin et al., 2016]. Appendix A also notes the obvious converse obstruction: if  $\varphi$  identifies two data objects, no downstream model can separate them. Appendix B discusses the scope of this universality statement and its distinction from sample efficiency or optimisation guarantees.

We now construct a faithful embedding of an irregular observation stream as a path. The construction is tailored to Log-NCDEs, which require interval log-signatures rather than pointwise values of an interpolated path. It therefore computes the required log-signatures directly from the observations, without interpolating the data. The procedure follows the signature-computation viewpoint of Morley and Lyons [2024]. We begin with an introduction to the tensor algebra, signatures, and log-signatures.

### 2.2 Tensor algebra, signatures, and log-signatures

Let  $X : [0, T] \rightarrow \mathbb{R}^{d_X}$  be a path of bounded variation, with coordinates  $X = (X^1, \dots, X^{d_X})$ . The signature of  $X$  over  $[s, t]$  records all iterated integrals of its coordinate increments,

$$S_{s,t}(X)^I = \int_{s < u_1 < \dots < u_k < t} dX_{u_1}^{i_1} \dots dX_{u_k}^{i_k}, \quad (1)$$

where  $I = i_1 \dots i_k$  is a word of length  $|I| = k$  with letters in  $\{1, \dots, d_X\}$  [Lyons et al., 2007, Friz and Victoir, 2010]. The empty word is denoted by  $\emptyset$ , with  $S_{s,t}(X)^\emptyset = 1$ . The  $k^{\text{th}}$  level consists of all signature coordinates  $S_{s,t}(X)^I$  indexed by words  $I$  of length  $k$ . The collection of all levels forms an element of the tensor algebra  $T((\mathbb{R}^{d_X}))$ , equipped with the product

$$(\mathbf{a} \otimes \mathbf{b})^I = \sum_{I=JK} \mathbf{a}^J \mathbf{b}^K, \quad (2)$$

where the sum is over all decompositions of  $I$  into two words  $J$  and  $K$ . The unit is  $\mathbf{1}$ , with  $\mathbf{1}^\emptyset = 1$  and  $\mathbf{1}^I = 0$  for  $|I| \geq 1$ . Chen’s identity [Chen, 1954] states that, for  $s \leq u \leq t$ ,

$$S_{s,t}(X) = S_{s,u}(X) \otimes S_{u,t}(X), \quad (3)$$

so this product is the algebraic counterpart of concatenating intervals [Chevyrev and Kormilitzin, 2016, McLeod and Lyons, 2025].

The tensor product is non-commutative, giving the Lie bracket  $[\mathbf{a}, \mathbf{b}] = \mathbf{a} \otimes \mathbf{b} - \mathbf{b} \otimes \mathbf{a}$ . The free Lie algebra  $\mathfrak{L}((\mathbb{R}^{d_x}))$  is generated by degree-one tensors under this bracket [Reutenauer, 1993]. The log-signature is defined

$$\log S_{s,t}(X) = \sum_{m=1}^{\infty} \frac{(-1)^{m+1}}{m} (S_{s,t}(X) - \mathbf{1})^{\otimes m} \quad (4)$$

and lives in  $\mathfrak{L}((\mathbb{R}^{d_x}))$  as signatures of bounded variation paths are group-like elements of  $T((\mathbb{R}^{d_x}))$  [Chen, 1957]. Although it contains the same information as the signature, each level is represented in the lower-dimensional free Lie algebra rather than in the full tensor algebra. The depth- $N$  truncated tensor algebra  $T^N(\mathbb{R}^{d_x})$  keeps only levels with degree at most  $N$ , and  $S_{s,t}^N(X)$  and  $\log S_{s,t}^N(X)$  are the projections of  $S_{s,t}(X)$  and  $\log S_{s,t}(X)$  onto these levels. We now introduce Log-NCDEs, which interact with the driving path on an interval through the truncated log-signature.

### 2.3 Neural controlled differential equations

An NCDE models a continuous-time hidden state  $h_t \in \mathbb{R}^{d_h}$  driven by a path  $X$  through a parametrised vector field  $f_\theta : \mathbb{R}^{d_h} \rightarrow \mathbb{R}^{d_h \times d_x}$  [Kidger et al., 2020],

$$dh_t = f_\theta(h_t) dX_t. \quad (5)$$

For  $a \in \mathbb{R}^{d_x}$ ,  $f_\theta(\cdot)a : \mathbb{R}^{d_h} \rightarrow \mathbb{R}^{d_h}$  denotes the vector field obtained by multiplying the matrix output of  $f_\theta$  by  $a$ . The vector field may be nonlinear, or may act linearly on the hidden state as in a Linear NCDE,  $f_\theta(h_t)dX_t = \sum_{i=1}^{d_x} A_\theta^i h_t dX_t^i$  [Cirone et al., 2024]. Predictions are produced from the hidden state by a readout map  $l_\psi$ . With a linear readout of the terminal hidden state, both nonlinear and Linear NCDEs are universal for continuous path-to-point maps [Kidger et al., 2020]. With a nonlinear readout of the hidden path, they are universal for continuous online path-to-path maps [Cirone et al., 2024]. Structured Linear CDEs (SLiCEs) restrict the matrices  $A_\theta^i$  to structured matrix families for efficiency. Several structures, including block-diagonal, diagonal-plus-low-rank, sparse, and the exponentially weighted signature retain the same path-to-point and path-to-path universality guarantees as dense Linear NCDEs [Walker et al., 2025, Movahedi et al., 2025, Bloch et al., 2026].

The Log-ODE method approximates CDE dynamics on an interval by constructing an autonomous ODE from the truncated log-signature of the driving path and the iterated Lie brackets of the vector fields [Castell and Gaines, 1995]. A Log-NCDE applies this approximation to NCDEs, so that the hidden-state evolution depends on the driving path only through its log-signature over intervals. Let  $\bar{f}_\theta$  be the Lie algebra homomorphism extending  $f_\theta$  from degree-one tensors to  $\mathfrak{L}^N(\mathbb{R}^{d_x})$ , so that  $\bar{f}_\theta(\cdot)a = f_\theta(\cdot)a$  for  $a \in \mathbb{R}^{d_x}$  and recursively

$$\bar{f}_\theta(\cdot)[a, b] = [\bar{f}_\theta(\cdot)a, \bar{f}_\theta(\cdot)b] = J_{\bar{f}_\theta(\cdot)b} \bar{f}_\theta(\cdot)a - J_{\bar{f}_\theta(\cdot)a} \bar{f}_\theta(\cdot)b, \quad (6)$$

where  $J_{\bar{f}_\theta(\cdot)b}$  denotes the Jacobian of the vector field  $\bar{f}_\theta(\cdot)b : \mathbb{R}^{d_h} \rightarrow \mathbb{R}^{d_h}$  and  $f_\theta$  needs to be  $\text{Lip}(\gamma)$  for  $\gamma \geq N$  [Walker et al., 2024]. On an interval  $[r_i, r_{i+1}]$ , the Log-ODE update solves

$$\frac{d\bar{h}_s}{ds} = \bar{f}_\theta(\bar{h}_s) \frac{\log S_{r_i, r_{i+1}}^N(X)}{r_{i+1} - r_i}, \quad s \in [r_i, r_{i+1}], \quad \bar{h}_{r_i} = h_{r_i}, \quad (7)$$

and sets  $h_{r_{i+1}} \approx \bar{h}_{r_{i+1}}$ .

For Linear NCDEs and SLiCEs, the interval flow has the closed-form  $\exp(\bar{A}_\theta(\log S_{s,t}^N(X)))$ , where  $\bar{A}_\theta$  is obtained from the matrices  $A_\theta^i$  by the same Lie-bracket construction, with vector-field brackets replaced by sign-flipped matrix commutators. Each interval acts on the hidden state by a linear map and the hidden states can be computed in parallel using an associative scan [Walker et al., 2025]. For SLiCEs, the efficiency of the chosen matrix structure is retained only when the Log-ODE construction

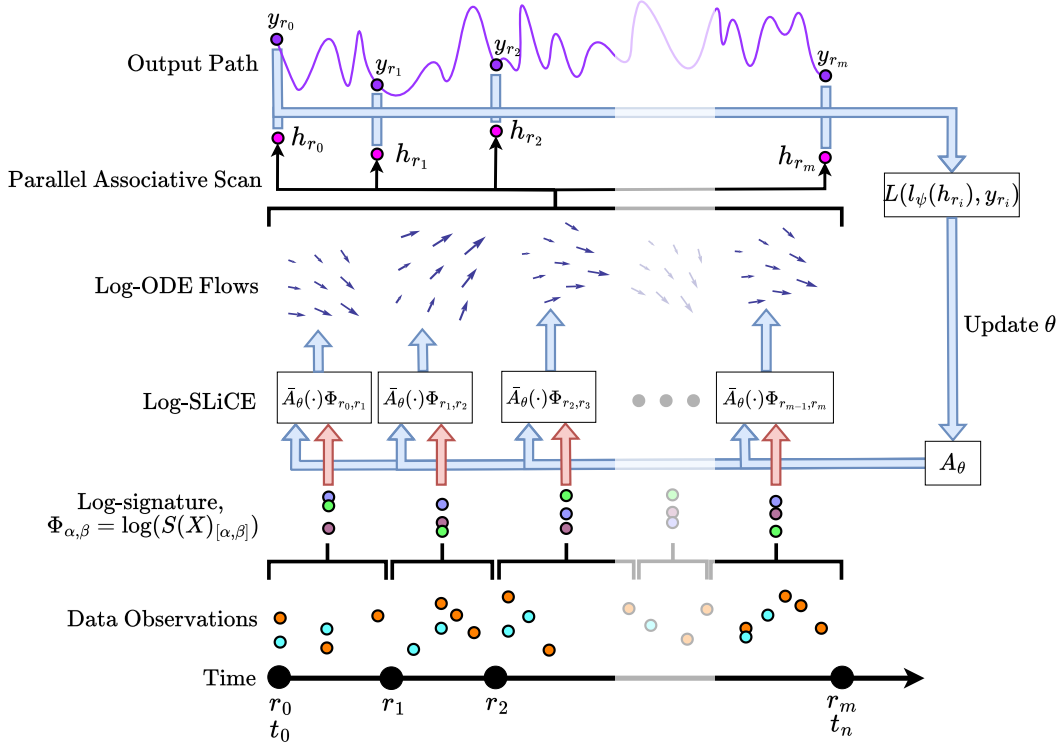


Figure 2: **Schematic of a Log-SLiCE.** Irregular observations are first summarised by interval log-signatures  $\Phi_{\alpha, \beta} = \log(S(X)_{[\alpha, \beta]})$ . The iterated Lie brackets of the matrices  $A_\theta^i$ , represented by  $\bar{A}_\theta$ , map each log-signature to a Log-ODE flow. These interval-wise hidden-state updates are composed using a parallel associative scan. The resulting hidden states  $h_{r_i}$  are decoded to produce estimates of the output values  $y_{r_i}$ , and the loss  $L(l_\psi(h_{r_i}), y_{r_i})$  is used to update the parameters.

remains inside that structure. This is true for block-diagonal SLiCEs, since block-diagonal matrices are closed under products, commutators, and matrix exponentials [Walker et al., 2025].

We refer to the resulting structure-preserving Log-ODE variant of SLiCE as Log-SLiCE. As shown in Section 3.1, Log-SLiCE reduces the time per training step by up to  $3,000\times$  on time series with roughly 18,000 observations when compared to standard NCDEs. Figure 2 illustrates the Log-SLiCE pipeline. The next section constructs the map from data observations to log-signatures over intervals.

## 2.4 From observations to log-signatures

Suppose we have  $d_{\text{disc}}$  channels for which we observe values at discrete times in  $[0, T]$ . We write the observation stream as

$$x = ((t_0, s_0, x_0), \dots, (t_n, s_n, x_n)), \quad 0 \leq t_0 < \dots < t_n \leq T, \quad (8)$$

where  $s_i \subseteq \{1, \dots, d_{\text{disc}}\}$  is the non-empty set of channels observed at time  $t_i$ , and  $x_i^k \in \mathbb{R}$  is the observed value of channel  $k \in s_i$ . The stream can be irregular and asynchronous, because the gaps  $t_{i+1} - t_i$  need not be equal and different subsets  $s_i$  can be observed at each time. Suppose we also have  $d_{\text{cont}}$  continuously observed channels for which we can access their value at any time, with time itself being the canonical example. The goal is to define a faithful path embedding of these continuous variables and observation streams, together with a procedure for efficiently computing the embedded path’s log-signature over any query interval, so that it can be used with Log-NCDEs. Rather than first constructing an interpolated path and then computing its log-signature, we define the interval log-signatures directly.

We first choose the coordinates of the path space. For an embedding to be injective, the construction must retain both the last recorded value of each discretely observed channel and whether a new

observation has occurred. We therefore use

$$d_X = 2d_{\text{disc}} + d_{\text{cont}}, \quad (9)$$

where the first  $d_{\text{disc}}$  coordinates give the current recorded values of the discretely observed channels, the next  $d_{\text{disc}}$  coordinates record observation counts in each channel, and the final  $d_{\text{cont}}$  coordinates store continuously observed variables. The count coordinates distinguish an observation that repeats the previous recorded value from the absence of a new observation in that channel. Where this distinction is irrelevant, the count coordinates can be omitted. The resulting embedding then intentionally identifies streams that differ only by the insertion or removal of value-preserving observations. This is a modelling choice, with the invariance-computational tradeoff discussed in Appendices A.5 and B.

We convert each observation into an increment in  $\mathbb{R}^{d_X}$ . For  $k \in s_i$ , let  $\text{prev}(i, k)$  be the most recent index  $j < i$  such that  $k \in s_j$ , i.e. the previous index where channel  $k$  is observed. We base-point augment the stream by setting  $x_{\text{prev}(i, k)}^k = 0$  if no such index exists. The event increment at time  $t_i$  is

$$\delta_i = \sum_{k \in s_i} \left[ \left( x_i^k - x_{\text{prev}(i, k)}^k \right) e_k + e_{d_{\text{disc}}+k} \right] \in \mathbb{R}^{d_X}, \quad (10)$$

where  $\{e_i\}_{i=1}^{d_X}$  is the standard basis of  $\mathbb{R}^{d_X}$ . Thus each observed channel contributes its change since its previous observation, together with a unit increment in its count coordinate.

Each  $\delta_i$  is then included into the truncated free Lie algebra. By default, we place  $\delta_i$  in degree one and set all higher-order components to zero,  $\Delta_i = (0, \delta_i, 0, \dots, 0) \in \mathfrak{L}^N(\mathbb{R}^{d_X})$ . This is where additional local information can be incorporated. For example, if an observation event includes precomputed signed-area terms, or if a local segment has known iterated integrals, these higher-order terms can be stored directly in  $\Delta_i$ . We provide an example of this for Brownian motion paths in Section 3.3. The corresponding signature factor associated with the observation event is  $E_i = \exp(\Delta_i) \in T^N(\mathbb{R}^{d_X})$ .

Let  $C : [0, T] \rightarrow \mathbb{R}^{d_{\text{cont}}}$  be a continuous path of bounded-variation representing the continuously observed variables, embedded in  $\mathbb{R}^{d_X}$  as  $\tilde{C}_t = (0, \dots, 0, C_t)$ , and write  $\Gamma_{u,v} = S_{u,v}^N(\tilde{C})$  and  $B_C = \exp(\tilde{C}_0)$ . For a query interval  $[\alpha, \beta)$  containing events  $\alpha \leq t_{i_1} < \dots < t_{i_m} < \beta$ , the signature over the interval is defined by

$$G_{\alpha, \beta}(x, C) = \begin{cases} B_C \otimes \Gamma_{\alpha, t_{i_1}} \otimes E_{i_1} \otimes \Gamma_{t_{i_1}, t_{i_2}} \otimes E_{i_2} \otimes \dots \otimes E_{i_m} \otimes \Gamma_{t_{i_m}, \beta}, & \alpha = 0, \\ \Gamma_{\alpha, t_{i_1}} \otimes E_{i_1} \otimes \Gamma_{t_{i_1}, t_{i_2}} \otimes E_{i_2} \otimes \dots \otimes E_{i_m} \otimes \Gamma_{t_{i_m}, \beta}, & \alpha > 0, \end{cases} \quad (11)$$

with  $B_C$  base-point augmenting  $C$ . Events at a right endpoint are assigned to the next interval, except that events at  $T$  are included in the final interval. The interval log-signature is

$$\Phi_{\alpha, \beta}(x, C) = \log G_{\alpha, \beta}(x, C) \in \mathfrak{L}^N(\mathbb{R}^{d_X}). \quad (12)$$

The Log-ODE method requires interval log-signatures on a partition  $\pi = \{0 = r_0 < r_1 < \dots < r_M = T\}$ , which we denote by  $\varphi_\pi(x, C) = (\Phi_{r_0, r_1}(x, C), \dots, \Phi_{r_{M-1}, r_M}(x, C))$ . The construction is depicted schematically in Figure 3.

Once the event increments have been formed, each interval can be processed independently and its factors composed in parallel using an associative scan, allowing for efficient computation. Furthermore, the construction is online, since for any  $\pi$ , the information needed to compute each  $\Phi_{r_i, r_{i+1}}(x, C)$  depends only on information up to time  $r_{i+1}$ . Thus the only remaining desired property is that these interval summaries arise from a faithful path embedding, since NCDEs and Log-NCDEs are universal models on path space. We therefore proceed by constructing a continuous path  $\Psi(x, C)$  whose interval log-signatures equal  $\Phi_{\alpha, \beta}(x, C)$  and which satisfies the following proposition.

**Proposition 2** (Faithfulness (informal)). *Assume the observation-count coordinates are included and that  $C$  contains time as a channel. Then the map  $(x, C) \rightarrow \Psi(x, C)$  is faithful.*

The construction of  $\Psi(x, C)$  and formal statement and proof of Proposition 2 are given in Appendix A.4. As with the rectilinear construction [Morrill et al., 2022], each observation event is assigned an interval of auxiliary time along which value and count coordinates move continuously while physical time is held fixed. Continuously observed variables contribute their signature factors over the physical-time gaps between events. Since signatures are invariant under reparametrisations of the auxiliary parameter, the durations assigned to these event intervals do not affect the resulting physical-time interval signatures.

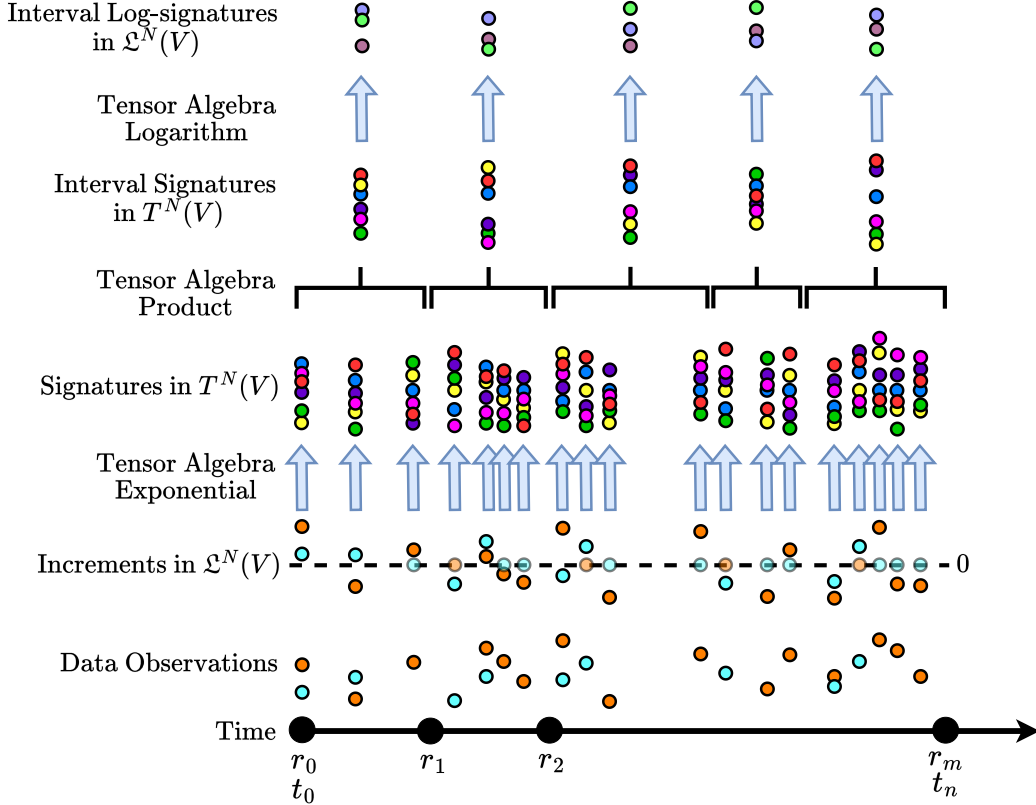


Figure 3: **Constructing interval log-signatures from irregular observations.** Each observation is converted into a Lie-algebra increment containing value increments and observation-count increments. Continuously observed variables, such as time, contribute signature factors over gaps between observations. Event and gap factors are composed over each query interval using a parallel associative scan with the tensor product, then mapped back to the free Lie algebra by the tensor logarithm. This gives interval log-signatures without interpolating the discretely observed channels.

### 3 Experiments

We evaluate our proposed embedding in four settings. First, we use EigenWorms, the longest dataset in the UEA multivariate time-series classification archive, to test the effect of the Log-ODE method on accuracy, speed, and GPU memory. Second, we test prediction on a synthetic sinusoidal system with output grids independent of input observation times. Third, we test prediction on a Brownian controlled system whose solution depends on second-order information. Fourth, we evaluate robustness on six UEA classification datasets under input dropping. The empirical scope is discussed further in Appendix B.

#### 3.1 Effect of the Log-ODE Method

Table 1 compares three NCDE models with and without the Log-ODE method on EigenWorms, holding all hyperparameters fixed to those selected by Walker et al. [2024] for NCDE and Log-NCDE. EigenWorms has 17,984 observations per series, making it a direct test of whether interval-level computation reduces the cost of long input sequences without sacrificing accuracy. Timing and memory measurements were run on an NVIDIA H100 GPU with a batch size of 1. Further experimental details are given in Appendix C.3.1. On this benchmark, every Log-ODE variant is faster and more accurate. Overall, combining the Log-ODE method with a SLICE increases test accuracy by 11.1 percentage points over a standard NCDE, while reducing the time per training step by a factor of almost 3,000. This cuts the time for 10,000 training steps from 3 days to 1.5 minutes.

Table 1: **NCDE models with and without the Log-ODE method on EigenWorms.** Results marked <sup>†</sup> are from Walker et al. [2024]; results marked <sup>‡</sup> are from Walker et al. [2025].

Model family	Log-ODE	Test Acc.	Time per step (s)	GPU Mem. (MB)
NCDE	×	75.0 ± 3.9 <sup>†</sup>	26.02	3484
	✓	85.6 ± 5.1 <sup>†</sup>	2.263	3494
LNCDE	×	87.2 ± 5.2	0.100	13730
	✓	88.3 ± 3.7 <sup>‡</sup>	0.018	3492
BD-SLiCE	×	81.1 ± 6.7	0.024	3494
	✓	86.1 ± 3.6 <sup>‡</sup>	0.009	3494

### 3.2 Synthetic coupled data

For a synthetic benchmark, we consider the multivariate system

$$\begin{aligned} z(t) &= \omega t + \phi, \\ x_i(t) &= A_i \sin(z(t) + \delta_i), \quad i = 1, \dots, d, \end{aligned} \quad (13)$$

where  $z$  is a shared latent phase which gives cross-channel structure. The parameters  $\omega$  and  $\phi$  are independently drawn per sample. The parameters  $A_i$  and  $\delta_i$  are sampled independently per channel. We fix  $d = 2$ . For further information on the set-up see Appendix C.1.

The observations are generated under four sampling regimes. The channels may be observed synchronously and regularly, synchronously and irregularly, asynchronously and irregularly, or at significantly different frequencies, where one channel is much sparser than the other.

For each sample, we draw a random query partition  $0 = q_0 < q_1 < \dots < q_m = T$ , where  $m$  varies between samples. We test whether models can learn the value at the end of each query interval  $[q_k, q_{k+1})$ , i.e.  $x(q_{k+1})$ , constructed from (13). This is not next-observation prediction since query endpoints need not coincide with observation times. The task therefore tests whether the model can use interval summaries to predict on an output grid chosen independently of the input sampling grid.

We first train one model for each data observation regime. Illustrative observation patterns and sample model outputs are shown in Figures 6–9 of Appendix C.1. We then evaluate these pre-trained models across the other regimes to assess cross-regime generalisation. Figure 4 reports the mean and standard deviation of this analysis. A model trained on synchronously observed, regularly sampled data struggles to generalise to asynchronously observed data in which one channel is sampled much more sparsely. This suggests that the model learns shortcuts when trained only on regularly sampled data. Conversely, because the asynchronous sparse regime is the hardest setting, a model trained on it remains robust across all other regimes. For irregularly sampled data, there is little difference between synchronous and asynchronous observations. This agrees with our view of faithful embeddings, since both regimes contain similar quantities of information and the model can learn to use it when it is faithfully represented. Figure 10 shows that their training curves are also very similar.

### 3.3 Linear system driven by Brownian motion

Next we test whether the model can exploit higher order information if it is available. We use precomputed Brownian rough paths, with the Lévy area computed as described by Jelinčič et al. [2025]. Each sample consists of a 4-dimensional Brownian stream on a fine regular grid (2048 observations between  $[0, 1]$ ), represented by log-signatures up to level 2, giving an input dimension of 10. These Brownian paths are used to drive a Stratonovich linear controlled system

$$dX_t = V_1 X_t \circ dW_t^1 + V_2 X_t \circ dW_t^2, \quad (14)$$

where  $V_1, V_2 \in \mathbb{R}^{r \times r}$  are fixed non-commuting matrices. Note that the CDE is only being controlled by two dimensions of the Brownian stream, therefore part of the task is to also learn which streams are redundant. We fix the dimension of the output path  $r = 2$ . The non-commutativity ensures that the solution depends not only on first-level Brownian increments, but also on second-level Lie bracket terms. The model predicts the state at the next query endpoint,  $y_k = X_{k+1}$ ,  $k = 0, \dots, m - 1$ .

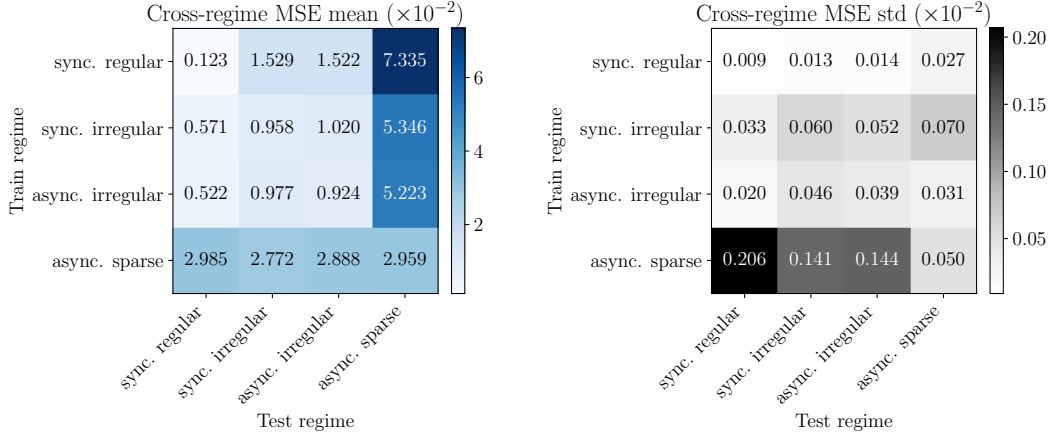


Figure 4: **Heatmap showing how well trained sinusoid models generalise across data sampling regimes.** The mean and standard deviation are computed over 5 random seeds.

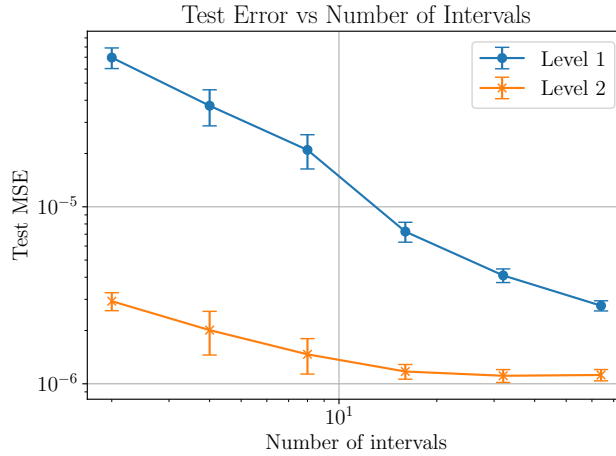


Figure 5: **Average test MSE against number of query intervals used for linear system driven by Brownian motion over 5 seeds.** As the system is driven by area information, we see a much lower MSE for when using level 2 log-signatures as we would expect, especially for fewer query intervals.

In Figure 5, we compare how our model performs when Lévy area information is provided compared with using only first level information, against the number of query intervals used. The solution depends intrinsically on second-level information, and we see that lower MSE is achieved with the higher order information. As the number of query intervals increase, the truncation error of using only first level decreases in magnitude, hence the test MSE decreases for the model trained on level 1. This highlights the flexibility of our approach in encompassing this additional information where it is available. Precise MSE averaged over 5 seeds can be seen in Table 3.

### 3.4 UEA input dropping

We evaluate robustness under input dropping on the six UEA time-series classification datasets chosen by Walker et al. [2024]. The comparison includes four structured recurrent baselines, S5 [Smith et al., 2023], LRU [Orvieto et al., 2023], S6, and Mamba [Gu and Dao, 2024], and an NCDE using Hermite cubic interpolation with backward differences [Kidger et al., 2020]. We test our proposed embedding using a Log-NCDE [Walker et al., 2024], diagonal Log-SLiCE (D-SLiCE), and block-diagonal Log-SLiCE (BD-SLiCE) [Walker et al., 2025]. For path-based models, we keep the original query windows fixed and recompute interval log-signatures from the remaining observations. Full details and per-dataset results are given in Appendix C.3.

Table 2: **Results on the six UEA datasets.** Average test accuracy (in %) and average dataset rank with no dropping and 30%, 70%, and 95% input dropping. Lower rank is better. No-drop values marked <sup>†</sup> are from Walker et al. [2024]; no-drop values marked <sup>‡</sup> are from Walker et al. [2025].

Model	No drop		30% drop		70% drop		95% drop	
	Av. Acc.	Av. Rank	Av. Acc.	Av. Rank	Av. Acc.	Av. Rank	Av. Acc.	Av. Rank
S5	61.8 <sup>†</sup>	4.67 <sup>†</sup>	63.4	3.25	60.1	4.83	56.7	5.33
LRU	61.7 <sup>†</sup>	4.50 <sup>†</sup>	60.9	5.58	61.0	5.00	60.8	<u>4.17</u>
S6	62.0 <sup>†</sup>	5.00 <sup>†</sup>	58.4	6.50	61.4	4.00	58.9	5.17
Mamba	58.6 <sup>†</sup>	6.67 <sup>†</sup>	59.5	4.83	60.6	4.00	57.6	6.17
NCDE	60.2 <sup>†</sup>	5.33 <sup>†</sup>	59.6	5.92	58.9	6.42	58.7	5.33
Log-NCDE	<b>64.3<sup>†</sup></b>	<u>3.00<sup>†</sup></u>	<b>64.2</b>	<u>3.08</u>	<b>62.7</b>	4.67	60.9	<u>4.17</u>
D-SLiCE	61.7 <sup>†</sup>	4.50 <sup>†</sup>	61.7	3.83	62.2	<u>3.83</u>	<u>62.2</u>	<b>2.83</b>
BD-SLiCE	<u>64.0<sup>‡</sup></u>	<b>2.33<sup>‡</sup></b>	<u>63.7</u>	<b>3.00</b>	<u>62.5</u>	<b>3.25</b>	<b>62.5</b>	<b>2.83</b>

Table 2 shows that the continuous-time models using our embedding are competitive across all dropping levels. Log-NCDE gives the best macro-average accuracy at no drop, 30% drop, and 70% drop. BD-SLiCE gives the best macro-average accuracy at 95% drop and the best or tied-best average rank at every dropping level. Its accuracy changes from 64.0% with no dropping to 62.5% with 95% dropping, indicating robustness under severe sparsification. These results show that the robustness of our approach is consistent across datasets and NCDE architectures.

## 4 Conclusion

This paper argues that continuous-time representations should preserve observed data rather than attempt to reconstruct unobserved behaviour. This principle is formalised through a general universality transfer result. For Hausdorff data and model input spaces, any continuous injective embedding transfers universality on compact sets from the model input space back to the data space. Thus, for a universal downstream model, an embedding need only be continuous and injective. Guided by this, we introduced a faithful embedding for irregular and partially observed streams tailored to Log-NCDEs. The construction records observations as tensor-algebra factors, composes them over arbitrary query intervals, and maps the result to interval log-signatures for use with the Log-ODE method. This approach avoids interpolation of observed variables, supports online prediction, decouples input observation times from output query times, and is computable in parallel over intervals and parallel-in-time within intervals. Experiments on synthetic controlled systems and UEA classification tasks show that the resulting models are accurate, efficient, and robust under irregularity, asynchrony, and severe input dropping.

## Acknowledgements

Benjamin Walker is supported by UK Research and Innovation (UKRI) through the Engineering and Physical Sciences Research Council (EPSRC) via Programme Grant [Grant No. UKRI1010: High order mathematical and computational infrastructure for streamed data that enhance contemporary generative and large language models] and CIMDA@Oxford, part of the AIR@InnoHK initiative funded by the Innovation and Technology Commission, HKSAR Government. Terry Lyons is supported by UK Research and Innovation (UKRI) through the Engineering and Physical Sciences Research Council (EPSRC) via Programme Grants [Grant No. UKRI1010: High order mathematical and computational infrastructure for streamed data that enhance contemporary generative and large language models], [Grant No. EP/S026347/1: Unparameterised multi-model data, high order signatures and the mathematics of data science], [Grant No. EP/Y028872/1: Mathematical Foundations of Intelligence: An Erlangen Programme for AI], and the UKRI AI for Science award [Grant No. UKRI2385: Creating Foundational Benchmarks for AI in Physical and Biological Complexity]. Terry Lyons is also supported by The Alan Turing Institute under the Defence and Security Programme (funded by the UK Government) and through the provision of research facilities; by the UK Government; and through CIMDA@Oxford, part of the AIR@InnoHK initiative funded by the Innovation and Technology Commission, HKSAR Government. The authors acknowledge support from His Majesty’s Government in the development of this research.

## References

- Anthony Bagnall, Hoang Anh Dau, Jason Lines, Michael Flynn, James Large, Aaron Bostrom, Paul Southam, and Eamonn Keogh. The UEA multivariate time series classification archive, 2018. *arXiv preprint, arXiv:1811.00075*, 2018.
- Torben Berndt, Benjamin Walker, Tiexin Qin, Jan Stühmer, and Andrey Kormilitzin. Permutation equivariant neural controlled differential equations for dynamic graph representation learning. In *Proceedings of the 39th Conference on Neural Information Processing Systems (NeurIPS)*, 2025.
- Alexandre Bloch, Samuel N. Cohen, Terry Lyons, Joël Mouterde, and Benjamin Walker. The exponentially weighted signature, 2026. URL <https://arxiv.org/abs/2603.19198>.
- Horatio Boedihardjo, Xi Geng, Terry Lyons, and Danyu Yang. The signature of a rough path: Uniqueness. *Advances in Mathematics*, 293:720–737, 2016.
- Jared Boyer, T. Konstantin Rusch, and Daniela Rus. Learning to dissipate energy in oscillatory state-space models. *arXiv preprint arXiv:2505.12171*, 2025.
- James Bradbury, Roy Frostig, Peter Hawkins, Matthew James Johnson, Chris Leary, Dougal Maclaurin, George Necula, Adam Paszke, Jake VanderPlas, Skye Wanderman-Milne, and Qiao Zhang. JAX: composable transformations of Python+NumPy programs, 2018.
- Fabienne Castell and Jessica Gaines. An efficient approximation method for stochastic differential equations by means of the exponential Lie series. *Mathematics and Computers in Simulation*, 38(1):13–19, 1995.
- Mihriban Ceylan, Anna P. Kwossek, and David J. Prömel. Universal approximation with signatures of non-geometric rough paths, 2026. URL <https://arxiv.org/abs/2602.05898>.
- Cristian Challu, Kin G Olivares, Boris N Oreshkin, Federico Garza Ramirez, Max Mergenthaler Canseco, and Artur Dubrawski. N-HITS: Neural hierarchical interpolation for time series forecasting. In *Proceedings of the AAAI conference on artificial intelligence*, volume 37, pages 6989–6997, 2023.
- Zhengping Che, Sanjay Purushotham, Kyunghyun Cho, David Sontag, and Yan Liu. Recurrent neural networks for multivariate time series with missing values. *Scientific Reports*, 8(1):6085, 2018.
- Kuo Tsai Chen. Iterated integrals and exponential homomorphisms. *Proceedings of the London Mathematical Society*, s3-4(1):502–512, 1954.
- Kuo Tsai Chen. Integration of paths, geometric invariants and a generalized Baker–Hausdorff formula. *Annals of Mathematics*, 65(1), 1957.
- Yuqi Chen, Kan Ren, Yansen Wang, Yuchen Fang, Weiwei Sun, and Dongsheng Li. ContiFormer: Continuous-time transformer for irregular time series modeling. In *Advances in Neural Information Processing Systems*, 2023.
- Ilya Chevyrev and Andrey Kormilitzin. A primer on the signature method in machine learning. *arXiv preprint arXiv:1603.03788*, 2016.
- Ilya Chevyrev, Emilio Ferrucci, Darrick Lee, Terry Lyons, Harald Oberhauser, and Nikolas Tapia. Orthogonal polynomials on path-space, 2026. URL <https://arxiv.org/abs/2602.18808>.
- Jeongwhan Choi and Noseong Park. Graph neural rough differential equations for traffic forecasting. *ACM Transactions on Intelligent Systems and Technology*, 14(4), 2023.
- Jeongwhan Choi, Hwangyong Choi, Jeehyun Hwang, and Noseong Park. Graph neural controlled differential equations for traffic forecasting. In *Proceedings of the 36th AAAI Conference on Artificial Intelligence (AAAI-22)*, 2022.
- Nicola Muca Cirone and Cristopher Salvi. Rough kernel hedging. *arXiv preprint arXiv:2501.09683*, 2025.
- Nicola Muca Cirone, Antonio Orvieto, Benjamin Walker, Cristopher Salvi, and Terry Lyons. Theoretical foundations of deep selective state-space models. In *Proceedings of the 38th Conference on Neural Information Processing Systems (NeurIPS)*, 2024.
- Thomas Cochrane, Peter Foster, Varun Chhabra, Maud Lemercier, Terry Lyons, and Cristopher Salvi. SK-Tree: a systematic malware detection algorithm on streaming trees via the signature kernel. In *2021 IEEE International Conference on Cyber Security and Resilience (CSR)*, pages 35–40. IEEE, 2021.

- Samuel N. Cohen, Silvia Lui, Will Malpass, Giulia Mantoan, Lars Nesheim, Áureo de Paula, Andrew Reeves, Craig Scott, Emma Small, and Lingyi Yang. Nowcasting with signature methods. *arXiv preprint arXiv:2305.10256*, 2023.
- Samuel N Cohen, James Foster, Peter Foster, Hang Lou, Terry Lyons, Sam Morley, James Morrill, Hao Ni, Edward Palmer, Bo Wang, Yue Wu, Lingyi Yang, and Weixin Yang. Subtle variation in sepsis-III definitions markedly influences predictive performance within and across methods. *Scientific Reports*, 14(1920), 2024.
- Christa Cuchiero, Francesca Primavera, and Sara Svaluto-Ferro. Universal approximation theorems for continuous functions of càdlàg paths and Lévy-type signature models, 2023. URL <https://arxiv.org/abs/2208.02293>.
- Edward De Brouwer, Jaak Simm, Adam Arany, and Yves Moreau. GRU-ODE-Bayes: Continuous modeling of sporadically-observed time series. In *Proceedings of the 33rd International Conference on Neural Information Processing Systems (NeurIPS)*, 2019.
- Jeffrey L. Elman. Finding structure in time. *Cognitive Science*, 14(2):179–211, 1990.
- Mónika Farsang, Radu Grosu, Ramin Hasani, and Daniela Rus. Parallelization of non-linear state-space models: Scaling up liquid-resistance liquid-capacitance networks for efficient sequence modeling. In *Proceedings of the 39th Conference on Neural Information Processing Systems (NeurIPS)*, 2025.
- Peter K Friz and Nicolas B Victoir. *Multidimensional stochastic processes as rough paths: theory and applications*, volume 120. Cambridge University Press, 2010.
- Albert Gu and Tri Dao. Mamba: Linear-time sequence modeling with selective state spaces. In *Proceedings of the First Conference on Language Modeling*, 2024.
- Albert Gu, Karan Goel, and Christopher Ré. Efficiently modeling long sequences with structured state spaces. In *Proceedings of The 10th International Conference on Learning Representations (ICLR)*, 2022.
- B. Hambly and T. Lyons. Uniqueness for the signature of a path of bounded variation and the reduced path group. *Annals of Mathematics*, 171:109–167, 2010.
- W. P. M. H. Heemels, K. H. Johansson, and P. Tabuada. An introduction to event-triggered and self-triggered control. In *Proceedings of the 51st IEEE Conference on Decision and Control*, 2012.
- Sepp Hochreiter and Jürgen Schmidhuber. Long short-term memory. *Neural Comput.*, 9(8):1735–1780, nov 1997. ISSN 0899-7667. doi: 10.1162/neco.1997.9.8.1735. URL <https://doi.org/10.1162/neco.1997.9.8.1735>.
- Christian Holberg and Cristopher Salvi. Exact gradients for stochastic spiking neural networks driven by rough signals. In *Proceedings of the 38th Conference on Neural Information Processing Systems (NeurIPS)*, 2024.
- Blanka Horvath, Maud Lemercier, Chong Liu, Terry Lyons, and Cristopher Salvi. Optimal stopping via distribution regression: A higher rank signature approach. *arXiv preprint arXiv:2304.01479*, 2023.
- Andraž Jelinčič, Jiajie Tao, William F. Turner, Thomas Cass, James Foster, and Hao Ni. Generative modeling of Lévy area for high order SDE simulation. *SIAM Journal on Mathematics of Data Science*, 7(4):1541–1567, 2025. doi: 10.1137/23M161077X. URL <https://doi.org/10.1137/23M161077X>.
- Sheo Yon Jhin, Jaehoon Lee, Minju Jo, Seungji Kook, Jinsung Jeon, Jihyeon Hyeong, Jayoung Kim, and Noseong Park. EXIT: Extrapolation and interpolation-based neural controlled differential equations for time-series classification and forecasting. In *Proceedings of the ACM Web Conference 2022, WWW '22*, page 3102–3112, New York, NY, USA, 2022. Association for Computing Machinery. ISBN 9781450390965. doi: 10.1145/3485447.3512030. URL <https://doi.org/10.1145/3485447.3512030>.
- Patrick Kidger, James Morrill, James Foster, and Terry Lyons. Neural Controlled Differential Equations for Irregular Time Series. In *Proceedings of the 34th Conference on Neural Information Processing System (NeurIPS)*, 2020.
- Franz J. Király and Harald Oberhauser. Kernels for sequentially ordered data. *Journal of Machine Learning Research*, 20(31):1–45, 2019.
- Kangjun Lee, Minha Kim, Youngho Jun, and Simon S. Woo. GDFlow: Anomaly detection with NCDE-based normalizing flow for advanced driver assistance system. *arXiv preprint arXiv:2409.05346*, 2024.
- Maud Lemercier, Cristopher Salvi, Thomas Cass, Edwin V Bonilla, Theodoros Damoulas, and Terry Lyons. SigGPDE: Scaling sparse gaussian processes on sequential data. In *International Conference on Machine Learning (ICML)*. PMLR, 2021a.

- Maud Lemerrier, Cristopher Salvi, Theodoros Damoulas, Edwin Bonilla, and Terry Lyons. Distribution regression for sequential data. In *International Conference on Artificial Intelligence and Statistics (AISTATS)*. PMLR, 2021b.
- Daniel Levin, Terry Lyons, and Hao Ni. Learning from the past, predicting the statistics for the future, learning an evolving system. *arXiv preprint arXiv:1309.0260*, 2016.
- Seonkyu Lim, Jeongwhan Choi, Noseong Park, Sang-Ha Yoon, ShinHyuck Kang, Young-Min Kim, and Hyunjoong Kang. Bridging dynamic factor models and neural controlled differential equations for nowcasting GDP. In *Proceedings of the 33rd ACM International Conference on Information and Knowledge Management*, 2024.
- Terry Lyons. Rough paths, signatures and the modelling of functions on streams. In *Proceedings of the International Congress of Mathematicians (ICM)*, volume 4, 2014.
- Terry J Lyons, Michael Caruana, and Thierry Lévy. *Differential Equations Driven by Rough Paths*. Springer, 2007.
- Georg Manten, Cecilia Casolo, Emilio Ferrucci, Søren Wengel Mogensen, Cristopher Salvi, and Niki Kilbertus. Signature kernel conditional independence tests in causal discovery for stochastic processes. In *Proceedings of the 13th International Conference on Learning Representations (ICLR)*, 2025.
- Farokh Marvasti, editor. *Nonuniform Sampling: Theory and Practice*. Kluwer Academic/Plenum Publishers, New York, 2001.
- Andrew McLeod and Terry Lyons. Signature methods in machine learning. *EMS Surveys in Mathematical Sciences*, 2025.
- P J Moore, T J Lyons, J Gallacher, and Alzheimer’s Disease Neuroimaging Initiative. Using path signatures to predict a diagnosis of Alzheimer’s disease. *PLoS One*, 14(9), 2019.
- Fernando Moreno-Pino, Álvaro Arroyo, Harrison Waldon, Xiaowen Dong, and Álvaro Cartea. Rough transformers: Lightweight and continuous time series modelling through signature patching. In *Proceedings of the 38th Conference on Neural Information Processing Systems (NeurIPS)*, 2024.
- Sam Morley and Terry Lyons. Roughpy: Streaming data is rarely smooth. In *Proceedings of the 23rd Python in Science Conference*, 2024.
- James Morrill, Andrey Kormilitzin, Alejo Nevado-Holgado, Sumanth Swaminathan, Sam Howison, and Terry Lyons. The signature-based model for early detection of sepsis from electronic health records in the intensive care unit. *Computing in Cardiology (CinC)*, 2019.
- James Morrill, Patrick Kidger, Lingyi Yang, and Terry Lyons. On the choice of interpolation scheme for neural CDEs. *Transactions on Machine Learning Research*, 2022(9), 2022.
- Sajad Movahedi, Felix Sarnthein, Nicola Muca Cirone, and Antonio Orvieto. Fixed-point RNNs: Interpolating from diagonal to dense. In *Proceedings of the 39th Conference on Neural Information Processing Systems (NeurIPS)*, 2025.
- Antonio Orvieto, Samuel L. Smith, Albert Gu, Anushan Fernando, Çağlar Gülçehre, Rázvan Pascanu, and Soham De. Resurrecting recurrent neural networks for long sequences. In *Proceedings of the 40th International Conference on Machine Learning (ICML)*, 2023.
- Adam Paszke, Sam Gross, Francisco Massa, Adam Lerer, James Bradbury, Gregory Chanan, Trevor Killeen, Zeming Lin, Natalia Gimelshein, Luca Antiga, Alban Desmaison, Andreas Köpf, Edward Yang, Zach DeVito, Martin Raison, Alykhan Tejani, Sasank Chilamkurthy, Benoit Steiner, Lu Fang, Junjie Bai, and Soumith Chintala. PyTorch: An imperative style, high-performance deep learning library. *arXiv preprint arXiv:1912.01703*, 2019.
- Barak A. Pearlmutter. Learning state space trajectories in recurrent neural networks. *Neural Computation*, 1(2): 263–269, 1989.
- Imanol Perez Arribas. Derivatives pricing using signature payoffs. *arXiv preprint arXiv:1809.09466*, 2018.
- Imanol Perez Arribas, Guy M Goodwin, John R Geddes, Terry Lyons, and Kate E A Saunders. A signature-based machine learning model for distinguishing bipolar disorder and borderline personality disorder. *Transl Psychiatry*, 8(1), 2018.

- Imanol Perez Arribas, Cristopher Salvi, and Lukasz Szpruch. Sig-SDEs model for quantitative finance. In *ACM International Conference on AI in Finance*, 2020.
- Tiexin Qin, Benjamin Walker, Terry Lyons, Hong Yan, and Haoliang Li. Learning dynamic graph embeddings with neural controlled differential equations. *IEEE Transactions on Pattern Analysis and Machine Intelligence*, 2025.
- Jeremy F. Reizenstein and Benjamin Graham. Algorithm 1004: The iisignature library: Efficient calculation of iterated-integral signatures and log signatures. *ACM Transactions on Mathematical Software*, 46(1):1–21, March 2020. doi: 10.1145/3371237.
- C. Reutenauer. *Free Lie Algebras*. London Mathematical Society Monographs. Clarendon Press, 1993.
- R. Rico-Martínez, K. Krischer, I. G. Kevrekidis, M. C. Kube, and J. L. Hudson. Discrete-vs. continuous-time nonlinear signal processing of Cu electrodisolution data. *Chemical Engineering Communications*, 118(1): 25–48, 1992.
- Yulia Rubanova, Tian Qi Chen, and David Kristjanson Duvenaud. Latent ordinary differential equations for irregularly-sampled time series. In *Proceedings of the 33rd International Conference on Neural Information Processing Systems (NeurIPS)*, 2019.
- T. Konstantin Rusch and Daniela Rus. Oscillatory state-space models. In *Proceedings of The 13th International Conference on Learning Representations (ICLR)*, 2025.
- Cristopher Salvi. *Rough paths, kernels, differential equations and an algebra of functions on streams*. PhD thesis, University of Oxford, 2021.
- Cristopher Salvi, Thomas Cass, James Foster, Terry Lyons, and Weixin Yang. The signature kernel is the solution of a Goursat PDE. *SIAM Journal on Mathematics of Data Science*, 3(3):873–899, 2021.
- Cristopher Salvi, Joscha Diehl, Terry Lyons, Rosa Preiss, and Jeremy Reizenstein. A structure theorem for streamed information. *Journal of Algebra*, 634:911–938, 2023.
- Nabeel Seedat, Fergus Imrie, Alexis Bellot, Zhaozhi Qian, and Mihaela van der Schaar. Continuous-time modeling of counterfactual outcomes using neural controlled differential equations. In *Proceedings of the 39th International Conference on Machine Learning (ICML)*, 2022.
- Daniil Shmelev and Cristopher Salvi. Sparse signature coefficient recovery via kernels. *arXiv preprint arXiv:2412.08579*, 2024.
- Satya Narayan Shukla and Benjamin M. Marlin. Interpolation-prediction networks for irregularly sampled time series. In *International Conference on Learning Representations*, 2019.
- Satya Narayan Shukla and Benjamin M. Marlin. Multi-time attention networks for irregularly sampled time series. In *International Conference on Learning Representations*, 2021.
- Jimmy T. H. Smith, Andrew Warrington, and Scott W. Linderman. Simplified state space layers for sequence modeling. In *Proceedings of The 11th International Conference on Learning Representations (ICLR)*, 2023.
- M. H. Stone. The generalized Weierstrass approximation theorem. *Mathematics Magazine*, 21(4):167–184, 1948.
- Ashish Vaswani, Noam Shazeer, Niki Parmar, Jakob Uszkoreit, Llion Jones, Aidan N. Gomez, Łukasz Kaiser, and Illia Polosukhin. Attention is all you need. In *Proceedings of the 31st Conference on Neural Information Processing Systems (NeurIPS)*, 2017.
- Andre Vauvelle, Paidi Creed, and Spiros Denaxas. Neural-signature methods for structured EHR prediction. *BMC Medical Informatics and Decision Making*, 22(1), 2022.
- Benjamin Walker, Andrew D. McLeod, Tiexin Qin, Yichuan Cheng, Haoliang Li, and Terry Lyons. Log neural controlled differential equations: The Lie brackets make a difference. In *Proceedings of the 41st International Conference on Machine Learning (ICML)*, 2024.
- Benjamin Walker, Lingyi Yang, Nicola Muca Cirone, Cristopher Salvi, and Terry Lyons. Structured linear CDEs: Maximally expressive and parallel-in-time sequence models. In *Proceedings of the 39th Conference on Neural Information Processing Systems (NeurIPS)*, 2025.
- Bo Wang, Maria Liakata, Hao Ni, Terry Lyons, Alejo J. Nevado-Holgado, and Kate Saunders. A Path Signature Approach for Speech Emotion Recognition. In *Proc. Interspeech 2019*, pages 1661–1665, 2019.

Jun Wang, Wenjie Du, Yiyuan Yang, Linglong Qian, Wei Cao, Keli Zhang, Wenjia Wang, Yuxuan Liang, and Qingsong Wen. Deep learning for multivariate time series imputation: A survey. In *Proceedings of the Thirty-Fourth International Joint Conference on Artificial Intelligence*, 2025.

Ernst Witt. Treue darstellung liescher ringe. *Journal für die reine und angewandte Mathematik*, 177:152–160, 1937.

Sihang Zeng, Lucas Jing Liu, Jun Wen, Meliha Yetisgen, Ruth Etzioni, and Gang Luo. Trajsurv: Learning continuous latent trajectories from electronic health records for trustworthy survival prediction. In *Proceedings of the Machine Learning for Healthcare (MLHC) Conference*, 2025.

## A Additional Details on Faithful Embeddings

This appendix gives the technical details behind the faithful-embedding criterion used in Section 2.1. The key point is that a continuous injective embedding preserves compact sets up to homeomorphism. Consequently, a universal function class on the embedded space can be pulled back to a universal function class on the original data space. We first prove the transfer result, then state the corresponding non-injectivity obstruction, and finally record the standard signature-universality consequence.

### A.1 Universality transfer

**Lemma 3** (Universality Transfer). *Let  $\mathcal{X}$  and  $\mathcal{P}$  be Hausdorff topological spaces, and let  $\varphi : \mathcal{X} \rightarrow \mathcal{P}$  be a continuous injection. Suppose  $\mathcal{F} \subseteq C(\mathcal{P}; \mathbb{R})$  is a family of continuous real-valued functions such that for every compact  $K \subseteq \mathcal{P}$ , the restrictions  $\mathcal{F}|_K$  are dense in  $C(K; \mathbb{R})$  in the uniform topology. Then for every compact  $K_0 \subseteq \mathcal{X}$ , the restrictions  $(\mathcal{F} \circ \varphi)|_{K_0}$  are dense in  $C(K_0; \mathbb{R})$  in the uniform topology, where*

$$\mathcal{F} \circ \varphi := \{f \circ \varphi : f \in \mathcal{F}\}.$$

*Proof.* Let  $K_0 \subseteq \mathcal{X}$  be compact, let  $f \in C(K_0; \mathbb{R})$ , and let  $\varepsilon > 0$ . Set  $K := \varphi(K_0) \subseteq \mathcal{P}$ . The continuous image of a compact set is compact, so  $K$  is compact. The restriction  $\varphi|_{K_0} : K_0 \rightarrow K$  is a continuous bijection from a compact space to a Hausdorff space, hence a homeomorphism. In particular,  $(\varphi|_{K_0})^{-1}$  is continuous.

Let

$$g := f \circ (\varphi|_{K_0})^{-1} : K \rightarrow \mathbb{R}.$$

Then  $g \in C(K; \mathbb{R})$ . By assumption,  $\mathcal{F}|_K$  is dense in  $C(K; \mathbb{R})$  in the uniform topology, so there exists  $h \in \mathcal{F}$  with

$$\sup_{p \in K} |g(p) - h(p)| < \varepsilon.$$

For every  $x \in K_0$ ,

$$g(\varphi(x)) = f((\varphi|_{K_0})^{-1}(\varphi(x))) = f(x).$$

Therefore

$$\sup_{x \in K_0} |f(x) - h(\varphi(x))| = \sup_{x \in K_0} |g(\varphi(x)) - h(\varphi(x))| = \sup_{p \in K} |g(p) - h(p)| < \varepsilon.$$

Since  $h \circ \varphi \in \mathcal{F} \circ \varphi$ , this proves that  $(\mathcal{F} \circ \varphi)|_{K_0}$  is dense in  $C(K_0; \mathbb{R})$ .  $\square$

The proof uses only the standard fact that a continuous bijection from a compact space to a Hausdorff space is a homeomorphism. In the main text,  $\mathcal{X}$  is the original data space,  $\mathcal{P}$  is the model input space, and  $\varphi$  is the embedding.

### A.2 Non-injectivity obstruction

We now record the complementary failure mode. If an embedding identifies two distinct data objects, then every downstream function of the embedding identifies them as well. Thus no downstream class can approximate continuous functions that separate those data objects.

**Proposition 4** (Non-faithfulness implies non-universality). *Let  $\mathcal{X}$  and  $\mathcal{P}$  be Hausdorff topological spaces, let  $\varphi : \mathcal{X} \rightarrow \mathcal{P}$  be a continuous map, and let  $\mathcal{F} \subseteq C(\mathcal{P}; \mathbb{R})$ . If  $\varphi$  is not injective on a compact  $K_0 \subseteq \mathcal{X}$ , then  $(\mathcal{F} \circ \varphi)|_{K_0}$  is not dense in  $C(K_0; \mathbb{R})$  in the uniform topology, where*

$$\mathcal{F} \circ \varphi := \{f \circ \varphi : f \in \mathcal{F}\}.$$

*Proof.* By assumption, there exist distinct  $x_1, x_2 \in K_0$  with  $\varphi(x_1) = \varphi(x_2)$ . Since  $K_0$  is compact Hausdorff, it is normal. Hence there exists  $f \in C(K_0; \mathbb{R})$  with  $f(x_1) \neq f(x_2)$ . Set

$$\varepsilon = \frac{|f(x_1) - f(x_2)|}{3}.$$

Let  $h \in \mathcal{F}$  be arbitrary. Since  $\varphi(x_1) = \varphi(x_2)$ , we have  $h(\varphi(x_1)) = h(\varphi(x_2))$ , and therefore

$$|f(x_1) - h(\varphi(x_1))| + |f(x_2) - h(\varphi(x_2))| \geq |f(x_1) - f(x_2)| = 3\varepsilon.$$

Hence one of the two summands is at least  $3\varepsilon/2 > \varepsilon$ , so

$$\sup_{x \in K_0} |f(x) - h(\varphi(x))| > \varepsilon.$$

Since  $h \in \mathcal{F}$  was arbitrary, no element of  $\mathcal{F} \circ \varphi$  approximates  $f$  to within  $\varepsilon$  on  $K_0$ . Thus  $(\mathcal{F} \circ \varphi)|_{K_0}$  is not dense in  $C(K_0; \mathbb{R})$ .  $\square$

Lemma 3 and Proposition 4 give the criterion used in the main text. Continuous and injective embeddings preserve universality on compact sets. Non-injective embeddings cannot preserve universality, because they discard information about the original data.

### A.3 Signature representations of data

Classical signature universality for paths has the same form as Lemma 3, after restricting to a class of paths on which the signature map is injective, or equivalently after quotienting by tree-like equivalence [Hambly and Lyons, 2010, Boedihardjo et al., 2016]. Recent work has also extended signature universality results to stochastic settings [Cuchiero et al., 2023, Ceylan et al., 2026, Chevyrev et al., 2026]. The following corollary records the same schema with paths replaced by data streams. Any continuous injection from data into the tensor algebra inherits universality through linear functionals.

**Corollary 5** (Universality of signature representations of data). *Let  $d, m, N \in \mathbb{N}$ , let*

$$T((\mathbb{R}^m)) = \prod_{k=0}^{\infty} (\mathbb{R}^m)^{\otimes k}$$

*be equipped with the product topology, and let  $G \subseteq T((\mathbb{R}^m))$  be the group-like elements with the subspace topology. Let  $\iota : (\mathbb{R}^d)^N \rightarrow G$  be a continuous injection. Then for every compact  $K_0 \subseteq (\mathbb{R}^d)^N$ , every continuous  $f : K_0 \rightarrow \mathbb{R}$ , and every  $\varepsilon > 0$ , there exists a continuous linear functional  $\ell$  on  $T((\mathbb{R}^m))$  depending on only finitely many tensor-algebra coordinates with*

$$\sup_{x \in K_0} |f(x) - \ell(\iota(x))| < \varepsilon.$$

*Proof.* Apply Lemma 3 with  $\mathcal{X} = (\mathbb{R}^d)^N$ ,  $\mathcal{P} = G$ ,  $\varphi = \iota$ , and  $\mathcal{F}$  the family of restrictions to  $G$  of finitely supported continuous linear functionals on  $T((\mathbb{R}^m))$ . The density hypothesis on  $\mathcal{F}$  follows from the shuffle identity and the real Stone-Weierstrass theorem, since these functionals contain the constants, separate points of  $G$ , and form an algebra on  $G$  [Reutenauer, 1993, Stone, 1948, Lyons, 2014].  $\square$

This is the same mechanism used in signature-based universality results. The only additional requirement is that the representation must separate the original data objects. For paths, this is the injectivity of the signature after removing tree-like equivalence. For data streams, it is the injectivity of the chosen embedding  $\iota$ .

Since linear functionals of signatures are universal on compact path classes once injectivity is established, truncated signature features provide expressive representations for statistical learning tasks [Levin et al., 2016]. Signature-based kernels extend this viewpoint to kernel methods on sequential data [Király and Oberhauser, 2019], while subsequent work develops learning directly with the full infinite-dimensional signature kernel [Salvi et al., 2021, Salvi, 2021, Lemercier et al., 2021b,a, Manten et al., 2025].

Signatures have a number of other useful properties, including that their iterated-integral coordinates are unchanged by translations of the path and by increasing reparameterisations of time [Chen, 1954]. Together with universality, these properties have led to their use across a wide range of domains, including healthcare [Perez Arribas et al., 2018, Moore et al., 2019, Wang et al., 2019, Morrill et al., 2019, Cohen et al., 2024, Vauvelle et al., 2022], quantitative finance [Perez Arribas, 2018, Perez Arribas et al., 2020, Horvath et al., 2023, Cirone and Salvi, 2025, Cohen et al., 2023], information theory [Salvi et al., 2023, Shmelev and Salvi, 2024], cybersecurity [Cochrane et al., 2021], and computational neuroscience [Holberg and Salvi, 2024].

Neural controlled differential equations extend this framework to learnable continuous-time models driven by paths, with applications including counterfactual prediction in healthcare [Seedat et al., 2022], economic nowcasting [Lim et al., 2024], survival prediction [Zeng et al., 2025], anomaly detection for driving assistance [Lee et al., 2024], dynamic graph learning [Qin et al., 2025, Berndt et al., 2025], and traffic forecasting [Choi et al., 2022, Choi and Park, 2023].

### A.4 Proof of faithfulness

We give a formal version of Proposition 2. The input consists of a continuously observed path  $C$  and an observation stream  $x$ . We assume throughout that  $C$  contains physical time as one of its channels.

Let  $\tau \in \{1, \dots, d_{\text{cont}}\}$  denote the continuous coordinate corresponding to physical time. Thus

$$C_t^\tau = t, \quad t \in [0, T].$$

Let  $C_{\text{BV}}^\tau$  be the space of bounded-variation paths

$$C : [0, T] \rightarrow \mathbb{R}^{d_{\text{cont}}}$$

satisfying this condition, equipped with the uniform topology.

For a fixed event pattern

$$\sigma = (s_0, \dots, s_{m-1}),$$

let  $\mathcal{X}_\sigma$  be the corresponding stream component. On this component, the number of events and the observed sets are fixed, while the event times and local event records vary. We equip each  $\mathcal{X}_\sigma$  with the standard product topology. We equip

$$\mathcal{X} = \coprod_{\sigma} \mathcal{X}_\sigma$$

with the disjoint-union topology. The joint input space is

$$\mathcal{D} = \mathcal{C}_{\text{BV}}^\tau \times \mathcal{X}.$$

For a stream with  $m$  events, set

$$I_m = [0, T + m + 1].$$

The target path space is

$$\mathcal{P} = \coprod_{m \geq 0} C(I_m, \mathbb{R}^{d_X}),$$

with the disjoint-union topology and the uniform topology on each component. The realised paths below lie in the bounded-variation subspace of  $\mathcal{P}$ .

We write  $o_i$  for the local record inserted at event  $i$ . For each observed set  $s$ , assume that local records are included through a continuous injective map

$$\iota_s : o \mapsto \Delta \in \mathfrak{L}^N(\mathbb{R}^{d_X}).$$

We assume that  $\Delta$  uses only the first  $2d_{\text{disc}}$  coordinates. We also assume that its degree-one count coordinates satisfy

$$\pi_1(\Delta)^{d_{\text{disc}}+k} = \mathbf{1}_{\{k \in s\}}.$$

Thus the count coordinates identify the observed set. For higher-order local information, the inserted object must be expressed in log-signature coordinates. If a local segment has a known truncated signature  $H$ , then the element stored as the event factor is

$$\Delta = \log H.$$

Assume that each local factor has a continuous bounded-variation realisation. For each observed set  $s$ , assume there is a continuous map

$$o \mapsto \eta_s(o)$$

from local records into bounded-variation paths

$$\eta_s(o) : [0, 1] \rightarrow \mathbb{R}^{d_X},$$

with the uniform topology, such that

$$\eta_s(o)(0) = 0, \quad S_{0,1}^N(\eta_s(o)) = \exp(\iota_s(o)).$$

We assume that  $\eta_s(o)$  uses only the first  $2d_{\text{disc}}$  coordinates. For event  $i$ , write

$$\Delta_i = \iota_{s_i}(o_i), \quad \eta_i = \eta_{s_i}(o_i).$$

The default construction in the main text is the special case

$$\Delta_i = \sum_{k \in s_i} \left[ \left( x_i^k - x_{\text{prev}(i,k)}^k \right) e_k + e_{d_{\text{disc}}+k} \right],$$

with all higher-order components equal to zero. In this degree-one case, one may take

$$\eta_i(u) = u \Delta_i.$$

On each fixed event-pattern component, replacing raw observed values by these value increments is a homeomorphism. The inverse is given by cumulative summation along each channel, starting from the fixed base point.

We now construct the path realisation. Fix

$$(C, x) \in \mathcal{D}, \quad x = ((t_0, s_0, o_0), \dots, (t_{m-1}, s_{m-1}, o_{m-1})).$$

Let  $\tilde{C}$  denote  $C$  embedded in the final  $d_{\text{cont}}$  coordinates of  $\mathbb{R}^{d_X}$ .

First define the initial auxiliary segment. For  $u \in I_m$ , set

$$\rho_*(u) = \min\{1, \max\{0, u\}\}.$$

This segment encodes the initial continuous value  $\tilde{C}_0$ . Its signature is

$$S_{0,1}^N(u \mapsto u \tilde{C}_0) = \exp(\tilde{C}_0) = B_C.$$

For each event  $i = 0, \dots, m-1$ , define

$$\rho_i^x(u) = \min\{1, \max\{0, u-1-t_i-i\}\}.$$

The function  $\rho_i^x$  is zero before the event segment for event  $i$ . It increases linearly from zero to one during that event segment. It is one after that event segment.

Define

$$q_x(u) = u - \rho_*(u) - \sum_{i=0}^{m-1} \rho_i^x(u).$$

The function  $q_x$  is used only to write the path explicitly. Since  $C$  contains physical time as a channel,  $q_x$  becomes the physical-time coordinate of the realised path.

Define

$$\Psi(x, C)(u) = \rho_*(u)\tilde{C}_0 + \left(\tilde{C}(q_x(u)) - \tilde{C}_0\right) + \sum_{i=0}^{m-1} \eta_i(\rho_i^x(u)).$$

This is a path in  $\mathbb{R}^{d_x}$ . At  $u = 0$ , the path starts at zero. During the initial auxiliary segment, the path moves from 0 to  $\tilde{C}_0$  while physical time is held fixed at 0. After the initial auxiliary segment, the continuously observed coordinates follow  $\tilde{C}(q_x(u))$ . During event segments, the continuously observed coordinates are held fixed while the event path  $\eta_i$  is traversed.

Since  $C_t^\tau = t$ , and since the event paths  $\eta_i$  use only the first  $2d_{\text{disc}}$  coordinates, the coordinate  $2d_{\text{disc}} + \tau$  of  $\Psi(x, C)$  is

$$\Psi(x, C)^{2d_{\text{disc}}+\tau}(u) = q_x(u).$$

Thus physical time is already one of the channels of  $\Psi(x, C)$ . During the initial auxiliary segment and during event segments, this time channel is constant. During ordinary parts of the path, this time channel increases at unit speed.

For a realised path  $\Psi = \Psi(x, C)$ , define

$$a_\Psi(t) = \inf \left\{ u \in I_m : \Psi^{2d_{\text{disc}}+\tau}(u) = t \right\}.$$

For  $\beta < T$ , define

$$b_\Psi(\beta) = a_\Psi(\beta).$$

For  $\beta = T$ , define

$$b_\Psi(T) = T + m + 1.$$

This final-endpoint convention includes events at  $T$  in the final interval.

For a physical-time interval  $[\alpha, \beta)$ , define

$$S_{\alpha, \beta}^N(\Psi) = S_{a_\Psi(\alpha), b_\Psi(\beta)}^N(\Psi).$$

This is the signature of the ordered auxiliary-time portion of  $\Psi$  whose time channel lies in  $[\alpha, \beta)$ , with events at  $T$  included when  $\beta = T$ .

**Proposition 6** (Formal faithfulness). *Assume the observation-count coordinates are included,  $C$  contains time as a channel, and  $N \geq 1$ . Under the local-factor assumptions above, the map*

$$(C, x) \mapsto \Psi(x, C)$$

*from  $\mathcal{D}$  to  $\mathcal{P}$  is continuous and injective. Moreover, for every  $0 \leq \alpha < \beta \leq T$ ,*

$$\log S_{\alpha, \beta}^N(\Psi(x, C)) = \Phi_{\alpha, \beta}(x, C).$$

*Proof.* We first prove the interval-signature identity. Let  $[\alpha, \beta)$  be a physical-time interval, with the same final-endpoint convention as in the main text. Suppose the events assigned to this interval are

$$\alpha \leq t_{i_1} < \dots < t_{i_r} < \beta,$$

with events at  $T$  included when  $\beta = T$ .

If  $\alpha = 0$ , then the selected auxiliary-time portion begins with the initial segment  $u \mapsto u\tilde{C}_0$ . The signature of this initial segment is

$$B_C = \exp(\tilde{C}_0).$$

The selected portion is then the ordered concatenation of this initial segment, the continuous pieces, and the event pieces. By Chen's identity,

$$S_{0, \beta}^N(\Psi(x, C)) = B_C \otimes \Gamma_{0, t_{i_1}} \otimes \exp(\Delta_{i_1}) \otimes \Gamma_{t_{i_1}, t_{i_2}} \otimes \exp(\Delta_{i_2}) \otimes \dots \otimes \exp(\Delta_{i_r}) \otimes \Gamma_{t_{i_r}, \beta}.$$

This is exactly  $G_{0,\beta}(x, C)$ .

If  $\alpha > 0$ , then the selected auxiliary-time portion does not include the initial segment. It is the ordered concatenation of the continuous pieces and event pieces

$$\tilde{C}|_{[\alpha, t_{i_1}], \eta_{i_1}, \tilde{C}|_{[t_{i_1}, t_{i_2}], \eta_{i_2}, \dots, \eta_{i_r}, \tilde{C}|_{[t_{i_r}, \beta]}.$$

Chen's identity gives

$$S_{\alpha,\beta}^N(\Psi(x, C)) = \Gamma_{\alpha, t_{i_1}} \otimes \exp(\Delta_{i_1}) \otimes \Gamma_{t_{i_1}, t_{i_2}} \otimes \exp(\Delta_{i_2}) \otimes \dots \otimes \exp(\Delta_{i_r}) \otimes \Gamma_{t_{i_r}, \beta}.$$

This is exactly  $G_{\alpha,\beta}(x, C)$ .

Therefore, for every  $0 \leq \alpha < \beta \leq T$ ,

$$\log S_{\alpha,\beta}^N(\Psi(x, C)) = \log G_{\alpha,\beta}(x, C) = \Phi_{\alpha,\beta}(x, C).$$

We now prove continuity. It is enough to work on a fixed event-pattern component. On such a component, the number of events and observed sets are fixed. Let

$$(C^{(j)}, x^{(j)}) \rightarrow (C, x)$$

in this component. Then

$$C^{(j)} \rightarrow C$$

uniformly, and for every event  $i$ ,

$$t_i^{(j)} \rightarrow t_i, \quad o_i^{(j)} \rightarrow o_i.$$

The map

$$a \mapsto \min\{1, \max\{0, u - a\}\}$$

is 1-Lipschitz uniformly in  $u$ . Hence

$$\|\rho_i^{x^{(j)}} - \rho_i^x\|_\infty \leq |t_i^{(j)} - t_i| \rightarrow 0.$$

It follows that

$$\|q_{x^{(j)}} - q_x\|_\infty \leq \sum_{i=0}^{m-1} \|\rho_i^{x^{(j)}} - \rho_i^x\|_\infty \rightarrow 0.$$

We control the initial continuous segment first. Since

$$C_0^{(j)} \rightarrow C_0,$$

we have

$$\sup_{u \in I_m} \|\rho_*(u) \tilde{C}_0^{(j)} - \rho_*(u) \tilde{C}_0\| \rightarrow 0.$$

We next control the continuously observed part after subtracting its initial value. Define

$$F_C(t) = \tilde{C}(t) - \tilde{C}_0.$$

Then

$$F_{C^{(j)}} \rightarrow F_C$$

uniformly. Since  $F_C$  is continuous on the compact interval  $[0, T]$ , it is uniformly continuous. Therefore

$$\begin{aligned} & \sup_{u \in I_m} \|F_{C^{(j)}}(q_{x^{(j)}}(u)) - F_C(q_x(u))\| \\ & \leq \|F_{C^{(j)}} - F_C\|_\infty + \sup_{u \in I_m} \|F_C(q_{x^{(j)}}(u)) - F_C(q_x(u))\|. \end{aligned}$$

The first term tends to zero by uniform convergence. The second term tends to zero by uniform continuity of  $F_C$  and the uniform convergence of  $q_{x^{(j)}}$  to  $q_x$ .

The local realisations depend continuously on the local records. Thus

$$\eta_i^{(j)} \rightarrow \eta_i$$

uniformly on  $[0, 1]$ . Since each  $\eta_i$  is uniformly continuous on  $[0, 1]$ , we have

$$\eta_i^{(j)}(\rho_i^{x^{(j)}}(\cdot)) \rightarrow \eta_i(\rho_i^x(\cdot))$$

uniformly. Combining the initial segment, the continuous part, and the event part gives

$$\|\Psi(x^{(j)}, C^{(j)}) - \Psi(x, C)\|_\infty \rightarrow 0.$$

Since the argument holds on each fixed event-pattern component, and since both the stream space and the target path space use disjoint-union topologies, the map

$$(C, x) \mapsto \Psi(x, C)$$

is continuous.

We now prove injectivity. The target component of  $\mathcal{P}$  determines the number of events  $m$ . The time coordinate

$$u \mapsto \Psi(x, C)^{2d_{\text{disc}} + \tau}(u)$$

is the function  $q_x(u)$ . Let

$$d_x(u) = u - q_x(u).$$

The initial auxiliary segment is the part where  $0 < d_x(u) < 1$ . For event  $i$ , the event segment is the closure of the set

$$\{u \in I_m : 1 + i < d_x(u) < 2 + i\}.$$

On this event segment, the time coordinate is constant and equal to  $t_i$ . Thus the realised path recovers all event times.

The final  $d_{\text{cont}}$  coordinates of  $\Psi(x, C)$  recover  $C$ . Indeed, after the initial auxiliary segment, the final  $d_{\text{cont}}$  coordinates are exactly

$$C(q_x(u)).$$

The event paths  $\eta_i$  use only the first  $2d_{\text{disc}}$  coordinates. The time coordinate  $q_x$  is surjective onto  $[0, T]$ . Therefore, for every  $t \in [0, T]$ , choosing any  $u \geq 1$  with  $q_x(u) = t$  recovers

$$C(t)$$

from the final  $d_{\text{cont}}$  coordinates of  $\Psi(x, C)(u)$ .

Now consider the event segment corresponding to event  $i$ . On this segment, the first  $2d_{\text{disc}}$  coordinates of  $\Psi(x, C)$  traverse  $\eta_i$ , up to translation by the previously completed event pieces. Signatures are invariant under translation. Therefore the signature of the event segment is

$$S_{0,1}^N(\eta_i) = \exp(\Delta_i).$$

Taking the truncated logarithm recovers

$$\Delta_i.$$

The degree-one count coordinates of  $\Delta_i$  recover the observed set  $s_i$ . Since

$$\Delta_i = \iota_{s_i}(o_i)$$

and  $\iota_{s_i}$  is injective, the local event record  $o_i$  is recovered by applying the inverse of  $\iota_{s_i}$  on its image.

In the default construction, the degree-one value coordinates of  $\Delta_i$  are

$$x_i^k - x_{\text{prev}(i,k)}^k, \quad k \in s_i.$$

Together with the recovered event order and observed sets, these increments recover the raw observed values recursively from the fixed base point. If

$$i_1 < i_2 < \dots < i_r$$

are the events at which channel  $k$  is observed, then

$$x_{i_\ell}^k = \sum_{j=1}^{\ell} \left( x_{i_j}^k - x_{\text{prev}(i_j,k)}^k \right).$$

Thus the full input  $(C, x)$  is uniquely determined by  $\Psi(x, C)$ . The path realisation is injective.  $\square$

## A.5 Invariance of the Embedding

The path realisation in Proposition 6 is faithful when count coordinates are included and  $C$  contains time as a channel. We describe two natural relaxations, dropping the count coordinates, and dropping the continuous variables, in terms of the invariances they induce in the corresponding log-signatures over intervals.

First suppose the count coordinates  $e_{d_{\text{disc}}+k}$  are dropped from the driving space, so that  $d_X = d_{\text{disc}} + d_{\text{cont}}$  and the discrete increment becomes

$$\delta_i = \sum_{k \in s_i} (x_i^k - x_{\text{prev}(i,k)}^k) e_k \in \mathbb{R}^{d_X}.$$

An observation event at time  $t_i$  with  $x_i^k = x_{\text{prev}(i,k)}^k$  for every  $k \in s_i$  contributes  $\delta_i = 0$ , hence  $E_i = \exp(0) = \mathbf{1}$ , and the chronological tensor product  $G_{\alpha,\beta}(x)$  is unaffected by the event's presence or absence.

Define the equivalence relation  $\sim_{\text{val}}$  on  $\mathcal{X}$  by  $x \sim_{\text{val}} x'$  if and only if  $x'$  is obtained from  $x$  by a finite sequence of insertions or removals of value-preserving observation events. Then  $G_{\alpha,\beta}(x) = G_{\alpha,\beta}(x')$  for every sub-interval  $[\alpha, \beta)$  whenever  $x \sim_{\text{val}} x'$ , so  $\varphi_\pi$  without count coordinates is an invariant of  $\mathcal{X} / \sim_{\text{val}}$  rather than of  $\mathcal{X}$ . The same holds true for the realised path embedding.

This is benign for streams in which value repeats carry no information. For continuous-valued sensor data, the set of streams with exact value repeats is measure-zero under any non-degenerate observation distribution, and a stream and its value-preserving insertions are typically indistinguishable for prediction purposes. For event-based discrete data, where value repeats are common and informative, for example a counter incremented at irregular times, or a binary state oscillating between two values, the equivalence class loses information that downstream tasks need, and count coordinates should be retained.

Now suppose the continuous variables are absent, so  $\mathbb{R}^{d_X} = \mathbb{R}^{2d_{\text{disc}}}$  (or  $\mathbb{R}^{d_{\text{disc}}}$  if count coordinates are also dropped). Then there are no gap factors  $\Gamma_{u,v}$ , and the interval signature reduces to a product of event factors,

$$G_{[\alpha,\beta)}(x) = \prod_{i: t_i \in [\alpha,\beta)} E_i.$$

The product depends only on which events fall in the interval and their order, not on the precise event times  $t_i$  themselves. An empty interval contributes  $\mathbf{1}$  regardless of length.

Define the equivalence relation  $\sim_{\text{time}}$  on  $\mathcal{X}$  by  $x \sim_{\text{time}} x'$  if and only if  $x'$  is obtained from  $x$  by changing event times  $\{t_i\}$  to any other strictly increasing sequence in  $[0, T]$ , with the same observed channel sets and values. Then  $G_{\alpha,\beta}(x) = G_{\alpha,\beta}(x')$  for every sub-interval  $[\alpha, \beta)$  that contains the same event indices in  $x$  and  $x'$ . For the partitioned encoding  $\varphi_\pi$ , this means  $\varphi_\pi(x) = \varphi_\pi(x')$  whenever  $x' \sim_{\text{time}} x$  and the event-to-interval assignments are preserved. For the realised path embedding, this means that the path consists only of auxiliary event segments. The gaps between events carry no path increment, so changing the event times only changes the allocation of these auxiliary segments to physical-time intervals; if that allocation is preserved, the interval signatures of the realised path are unchanged.

The timestamps remain in the data stream as metadata, used to specify query intervals and to drive downstream continuous-time models, but they no longer enter the encoding itself. This is appropriate when the modelling task is concerned with the sequence of events and their values, not with the precise inter-event timings; for example, in classification problems where temporal regularity is irrelevant, or in event-driven control problems where only the event ordering matters. When precise timing information is needed, physical time should be included as a continuous variable.

## B Limitations

This section clarifies the main assumptions and scope of the proposed embedding and experiments.

The first limitation concerns the faithful embedding itself. Proposition 6 assumes that observation-count coordinates are included and that physical time is present as a continuous channel. The count coordinates increase the dimension of the driving path, from  $d_{\text{disc}} + d_{\text{cont}}$  to  $2d_{\text{disc}} + d_{\text{cont}}$ . This increases the size of the truncated tensor and log-signature representations. For truncation depth  $N$ , the number of tensor coordinates up to depth  $N$  scales as  $\sum_{k=1}^N d_X^k = O(d_X^N)$ . Although the log-signature dimension is smaller, scaling like  $O(d_X^N/N)$  by the Witt formula [Witt, 1937, Reizenstein and Graham, 2020], this still grows exponentially in  $N$ . Thus enforcing exact injectivity through auxiliary channels can increase computational cost, especially for high-dimensional streams or high truncation depths. As discussed in Appendix A.5, omitting count coordinates or physical time is a modelling choice that intentionally introduces invariances. This can be appropriate when repeated observations or exact timestamps are not informative, but it can discard information in event-based or timing-sensitive tasks.

The second limitation concerns the interpretation of universality. The universality result is a compact-set approximation result and should not be interpreted as a guarantee of sample efficiency, optimisation success, or improved performance on every dataset. It shows that a continuous injective embedding does not obstruct approximation by a universal downstream model. The empirical behaviour still depends on the model class, truncation depth, optimisation procedure, data distribution, and availability of informative observations.

The final limitation concerns empirical scope. Our experiments cover synthetic controlled systems and six UEA time-series classification datasets, including robustness to input dropping. They do not exhaust all irregular, asynchronous, sparse, or event-based data regimes. The Brownian experiment assumes that second-order information, such as Lévy area, is available or precomputed.

## C Further details on experiments

Single runs for all experiments can be completed on a 24GB NVIDIA RTX 4090 GPU in less than 24 hours. We use the following publicly available datasets, libraries, and baseline models:

- **UEA Multivariate Time Series Classification Archive** Bagnall et al. [2018]. License: GPL-3.0.  
URL: <https://www.timeseriesclassification.com/>, <https://github.com/time-series-machine-learning/tsml-repo>
- **S5** Smith et al. [2023]. License: Apache 2.0.  
URL: <https://github.com/lindermanlab/S5>
- **LRU** Orvieto et al. [2023]. License: MIT.  
URL: <https://github.com/NicolasZucchet/minimal-LRU>
- **S6/Mamba** Gu and Dao [2024]. License: Apache 2.0.  
URL: <https://github.com/state-spaces/mamba>
- **Log-NCDE** Walker et al. [2024]. License: CC-BY-4.0  
URL: <https://github.com/Benjamin-Walker/log-neural-cdes>
- **JAX** Bradbury et al. [2018]. License: Apache 2.0.  
URL: <https://github.com/google/jax>
- **PyTorch** Paszke et al. [2019]. License: BSD Style, see here [https://github.com/pytorch/pytorch/pytorch?tab=License-1-ov-file](https://github.com/pytorch/pytorch?tab=License-1-ov-file)  
URL: <https://github.com/pytorch/pytorch>

### C.1 Synthetic coupled data

This section gives further experimental details for the synthetic coupled experiment described in Section 3.2. Each sample is generated on the time interval  $[0, T]$  with terminal time  $T = 10$  and observed channels  $d = 2$ . We restate the underlying continuous-time signal for ease of reference

$$z(t) = \omega t + \phi, \quad x_i(t) = A_i \sin(z(t) + \delta_i), \quad i = 1, \dots, d.$$

For each sample, the shared angular frequency and global phase are drawn as

$$\omega \sim \mathcal{U}(0.8, 1.6), \quad \phi \sim \mathcal{U}(0, 2\pi),$$

and the channel-specific parameters are sampled independently as

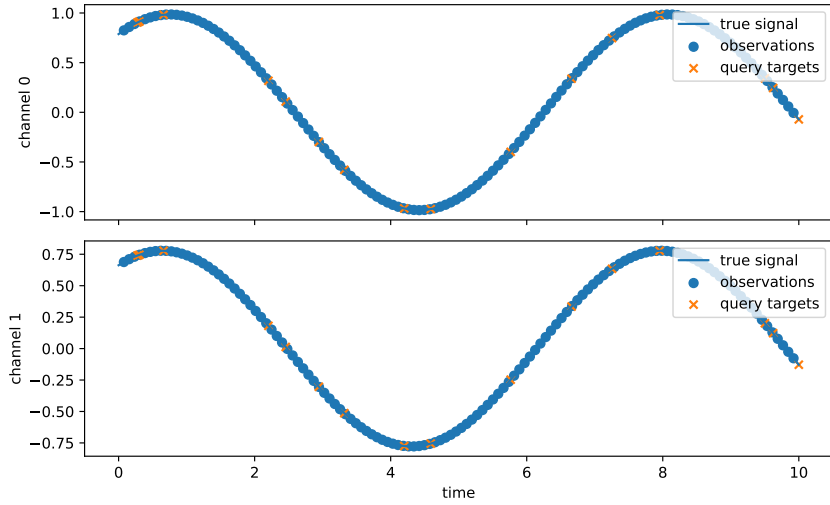
$$A_i \sim \mathcal{U}(0.7, 1.3), \quad \delta_i \sim \mathcal{U}(0, 2\pi).$$

The shared latent phase  $z(t)$  induces dependence between the two channels, while the channel-specific amplitudes and phase offsets prevent the task from reducing to identical copies of a one-dimensional signal. No observation noise is added in this experiment.

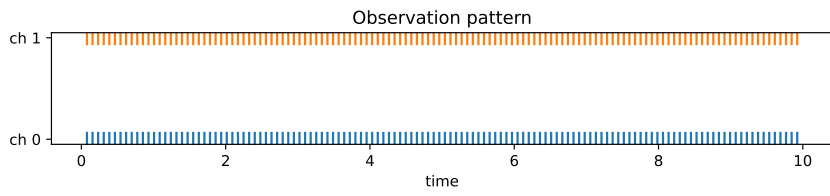
The observations are taken in  $(0, T)$  and the target values are computed directly from the underlying continuous dynamics rather than from the observed samples. We evaluate four observation regimes. In the *synchronous regular* regime, both channels are observed at the same fixed regular grid of 128 interior time points. In the *synchronous irregular* regime, a single irregular observation grid is sampled and shared by both channels. The grid is generated by a Poisson process with rate  $\lambda \sim \mathcal{U}(8, 10)$  per unit time, which means an expected 80–100 samples over  $[0, T]$ . In the *asynchronous irregular* regime, each channel has its own independently sampled Poisson observation grid, again with channel-wise rate  $\lambda_i \sim \mathcal{U}(8, 10)$ . Finally, in the *asynchronous sparse* regime, channels are observed asynchronously but at substantially different frequencies. The first channel is dense and second channel is sparse. Dense channels use rates  $\lambda_i \sim \mathcal{U}(12, 20)$ , while sparse channels use rates  $\lambda_i \sim \mathcal{U}(2, 4)$ . In all cases where we sample from Poisson process, if a channel has fewer than two observations, two observation times are sampled uniformly from  $(0, T)$  as a fallback. This guarantees that every channel is observed at least twice.

Figures 6–9 show samples from the four regimes. The synchronous regular case (Figure 6) has a fixed common input grid, the synchronous irregular case (Figure 7) has an irregular but shared input grid, the asynchronous irregular case (Figure 8) has independent irregular grids, and the asynchronous sparse case (Figure 9) combines asynchronous observation with a big difference in observation frequency across the channels.

We convert the observation stream to the increment representation. In this experiment we do not include observation-count coordinates in the model input, since the sampled sinusoid observations almost surely do not contain exact repeated event values. Physical time is appended as a continuously observed channel. Thus the model input has  $d + 1 = 3$  channels: two discretely observed value-increment channels and one continuously observed time channel.

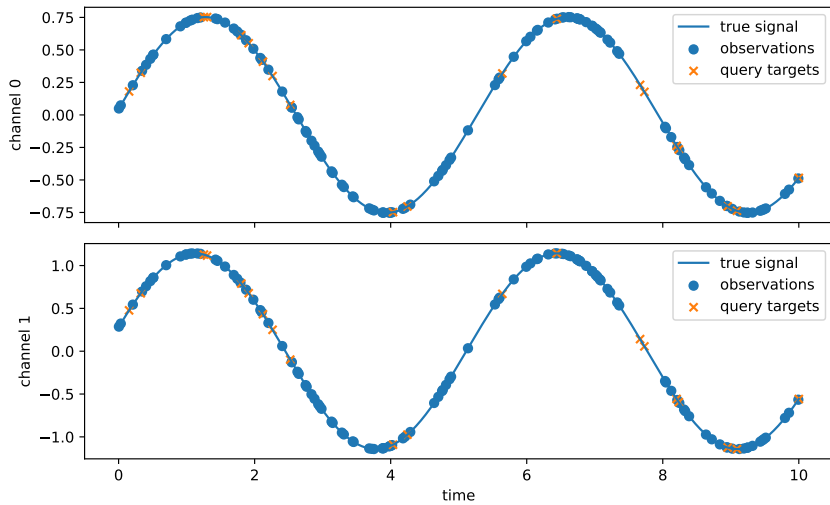


(a) True underlying signal, observation, and query targets.

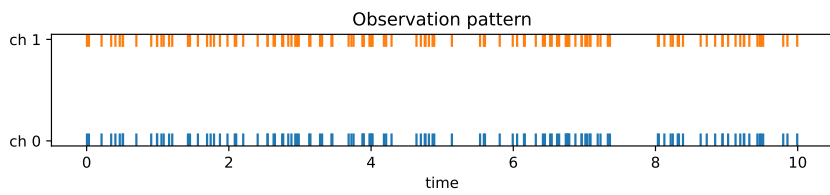


(b) Observation pattern of the two channels.

Figure 6: **Observation patterns and signal example for synchronous regular regime.**

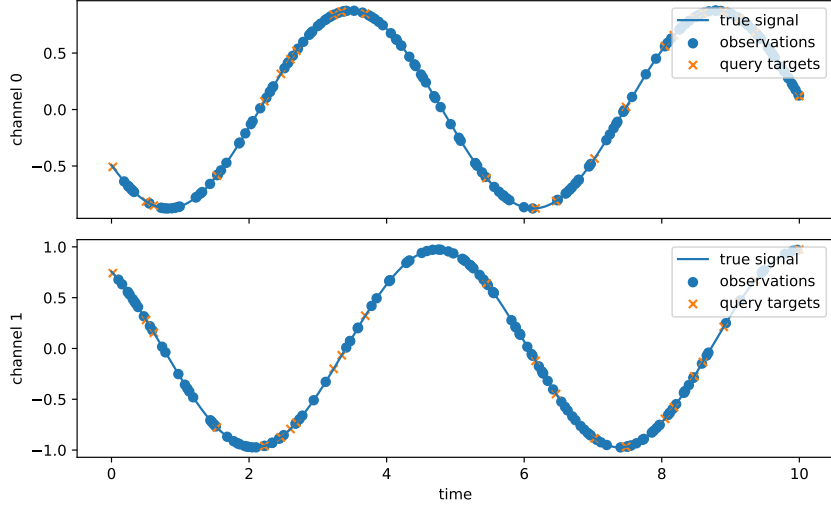


(a) True underlying signal, observation, and query targets.

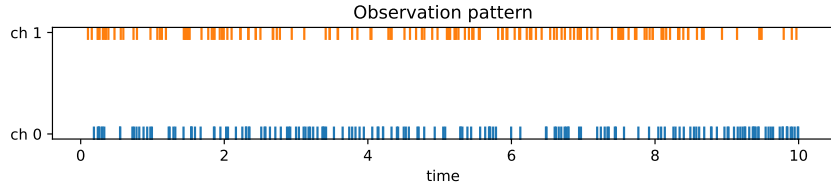


(b) Observation pattern of the two channels.

Figure 7: **Observation patterns and signal example for synchronous irregular regime.**



(a) True underlying signal, observation, and query targets.



(b) Observation pattern of the two channels.

Figure 8: **Observation patterns and signal example for asynchronous irregular regime.**

For each sequence, we also store the first observed value in each channel. This vector is passed to the input-dependent initialisation of the controlled differential equation after a tanh transformation. This gives the model access to the starting observed level of each channel while the subsequent path records increments from one observation to the next.

For every sample, we draw an output query partition independently of the observation times with the number of query intervals  $m$  sampled uniformly from  $\{16, 17, \dots, 32\}$ . We then sample  $m - 1$  interior query points uniformly from  $(0, T)$ , sort them, and append the endpoints 0 and  $T$ , giving

$$0 = q_0 < q_1 < \dots < q_m = T.$$

The model receives the log-signature of the observed stream over each interval  $[q_k, q_{k+1})$  and is trained to predict the true endpoint value

$$y_k = x(q_{k+1}) \in \mathbb{R}^2.$$

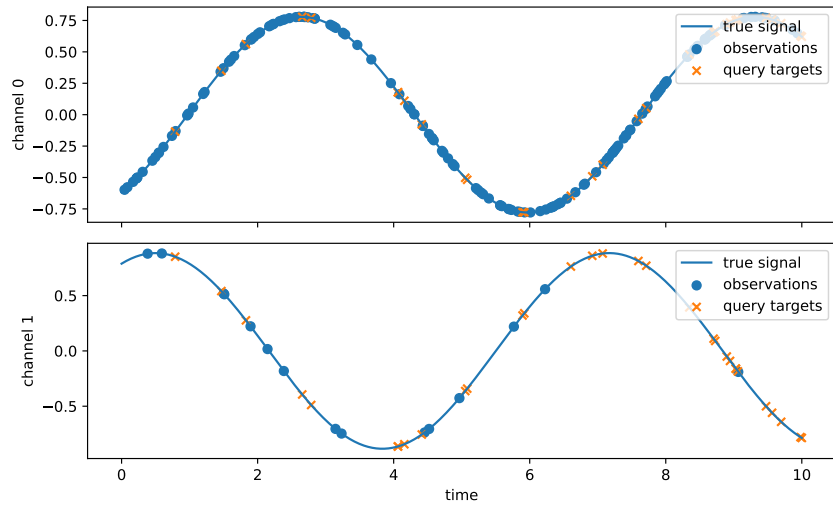
Since  $q_{k+1}$  is not required to be an observation time, the task is therefore not next-observation prediction. It tests whether the interval summaries allow the model to predict the underlying state on an output grid chosen independently of the input sampling grid.

We train one model on data generated from each observation regime. Each training set contains 2048 samples and each test set contains 512 samples. We use batch size 32 and train for 100 epochs. The model is a block diagonal log-SLiCE with hidden dimension 64, log-signature depth 2, block size 8. A linear decoder is applied to the hidden state at each query interval to produce the two-dimensional prediction. We optimise the mean squared error over all non-padded query intervals using Adam with learning rate  $10^{-3}$  and global gradient clipping at norm 1.

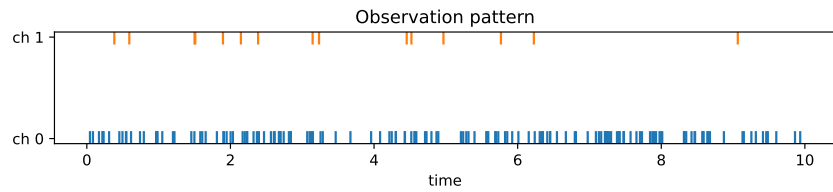
Because the number of query intervals varies between samples, interval targets are padded within each batch. The loss is computed only on valid intervals. If  $\hat{y}_{b,k}$  and  $y_{b,k}$  denote the prediction and target for sample  $b$  and interval  $k$ , and  $m_{b,k} \in \{0, 1\}$  is the padding mask, the training objective is

$$\mathcal{L} = \frac{\sum_{b,k} m_{b,k} \|\hat{y}_{b,k} - y_{b,k}\|_2^2}{d_{\text{out}} \sum_{b,k} m_{b,k}},$$

where  $d_{\text{out}} = 2$  is the number of predicted channels.



(a) True underlying signal, observation, and query targets.



(b) Observation pattern of the two channels.

Figure 9: Observation patterns and signal example for asynchronous sparse regime.

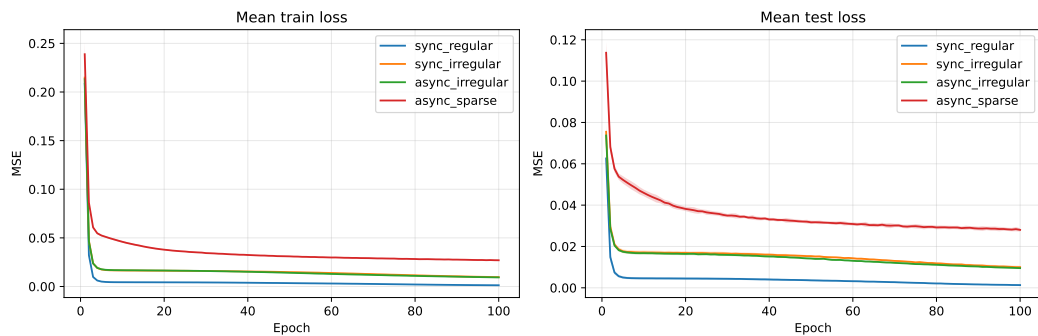


Figure 10: Training/test loss over epochs for the synthetic coupled task.

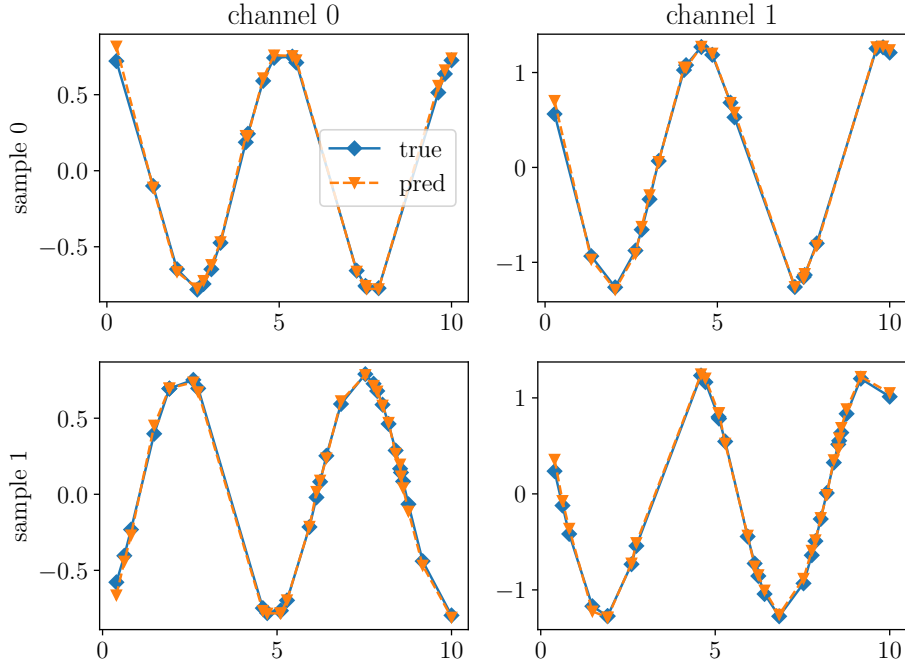


Figure 11: **Prediction examples for model trained on synchronous regular data.**

After training one model on each regime, we evaluate each trained model on test sets from all four regimes. This gives the cross-regime matrix seen in Figure 4, which reports the mean and standard deviation of the test MSE across five repeats, scaled by  $10^{-2}$ .

This cross-regime protocol is designed to test sampling-regime robustness. A model trained only on synchronous regular data can exploit the fixed sampling structure seen during training, and therefore achieves very low error on the matching test regime. However, this does not transfer well to irregular, asynchronous, or sparse observations. In contrast, the asynchronous sparse regime is the hardest training distribution because it exposes the model to asynchronous observations with unequal inter-observation gaps, and severe imbalance in observation frequency. Models trained in this regime therefore generalise more robustly to the other regimes, as shown by the more consistent off-diagonal errors in the final row of Figure 4. The similarity between the synchronous irregular and asynchronous irregular rows is consistent with the training curves in Figure 10. If the input grid is irregular, making the two channels asynchronous does not substantially change the difficulty of the task for our model.

In Figures 11–14, we see example outputs from trained models under different data sampling regimes. The predictions closely track the sinusoidal targets in most cases. In the asynchronous sparse case, note that channel 1 is the sparsely observed channel, hence the larger error for Figure 14.

## C.2 Linear system driven by Brownian motion

This section gives the full experimental details for the Brownian controlled system in Section 3.3. This experiment tests whether our Log-SLiCEs can exploit higher-order information when it is present in the data. The solution of the system considered here depends on second-order Lie bracket information.

We use a precomputed ensemble of 4-dimensional Brownian rough paths on the interval  $[0, 1]$ . Each path is stored on a fine regular grid with 2048 time steps. The stored input at each step is a truncated log-signature increment up to depth 2, and so this is of dimension 10. That is, each Brownian sample is represented by an array of shape  $2048 \times 10$ .

For each Brownian path, we construct targets by simulating a two-dimensional linear controlled system driven by the first two Brownian coordinates, with initial state  $X_0 = (1, 0)^\top \in \mathbb{R}^2$ .

$$dX_t = V_1 X_t \circ dW_t^1 + V_2 X_t \circ dW_t^2,$$

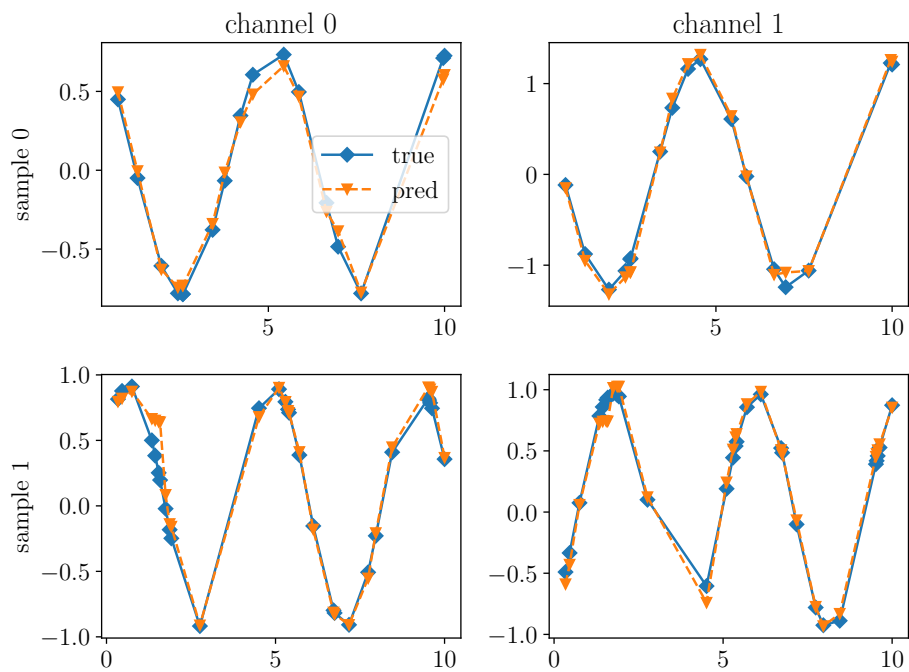


Figure 12: Prediction examples for model trained on synchronous irregular data.

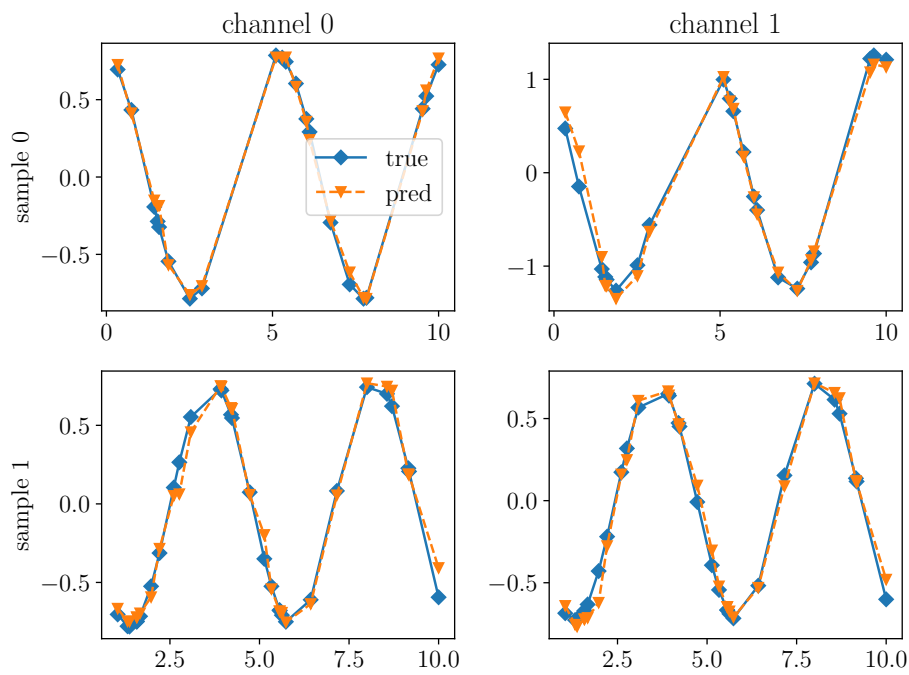


Figure 13: Prediction examples for model trained on asynchronous irregular data.

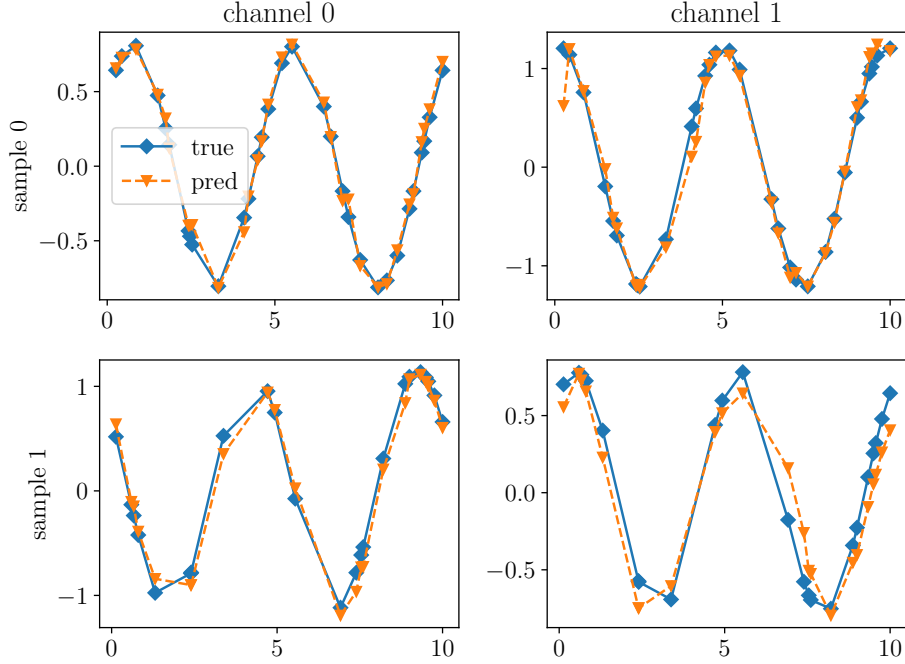


Figure 14: **Prediction examples for model trained on asynchronous sparse data.**

The two degree-one vector fields are fixed linear maps

$$V_1 = 0.15 \begin{pmatrix} -0.5 & -1.0 \\ 1.0 & -0.5 \end{pmatrix}, \quad V_2 = 0.15 \begin{pmatrix} -0.2 & 0.8 \\ 0.3 & -0.7 \end{pmatrix}.$$

The use of non-commuting matrices here ensures that second-order information cannot be removed without changing the solution.

Although these Brownian streams are four-dimensional, our target system here is driven only by the first two Brownian coordinates. The remaining coordinates are therefore irrelevant for the target dynamics and must be ignored by the model.

We loop over a number of query intervals

$$m \in \{2, 4, 8, 16, 32, 64\}.$$

The interval endpoints are aligned with the fine Brownian grid. For a given random seed, we sample  $m - 1$  cut indices uniformly without replacement from the interior grid indices, sort them, and append the endpoints 0 and 2048. After rescaling by 2048, this gives a random partition

$$0 = q_0 < q_1 < \dots < q_m = 1.$$

The same partition is used for all samples within a run. The target associated with interval  $[q_k, q_{k+1})$  is the simulated state at the right endpoint,

$$y_k = X(q_{k+1}) \in \mathbb{R}^2.$$

Although the model predicts endpoint values on a query grid that is separate from the fine input grid, the query endpoints are chosen to coincide with fine-grid points to make use of the available second level information.

When only depth-1 information is used, we keep only the first four coordinates, i.e. the Brownian increments themselves. In both cases, physical time is appended as a continuously observed channel. Therefore the model input has  $10 + 1 = 11$  channels in the depth-2 setting and  $4 + 1 = 5$  channels in the depth-1 setting.

We use block diagonal Log-SLiCE with hidden dimension 64 and block size 8. A linear decoder maps the hidden state at each query interval to the two-dimensional predicted state. Unlike the sinusoid experiment, we do not use input-dependent initialisation in this experiment.

Each run uses 2048 training paths and 512 test paths. We train with batch size 32 for 40 epochs using Adam with learning rate  $10^{-3}$  and global gradient clipping at norm 1. For each value of  $m \in \{2, 4, 8, 16, 32, 64\}$ , we

Table 3: **Test MSE versus number of intervals.** All values are scaled by  $10^{-6}$  and reported as mean  $\pm$  standard deviation across 5 seeds.

Intervals	Level 1	Level 2
2	$6.97 \pm 0.93$	$0.29 \pm 0.03$
4	$3.72 \pm 0.86$	$0.20 \pm 0.06$
8	$2.10 \pm 0.46$	$0.15 \pm 0.03$
16	$0.72 \pm 0.09$	$0.12 \pm 0.01$
32	$0.41 \pm 0.04$	$0.11 \pm 0.01$
64	$0.28 \pm 0.02$	$0.11 \pm 0.01$

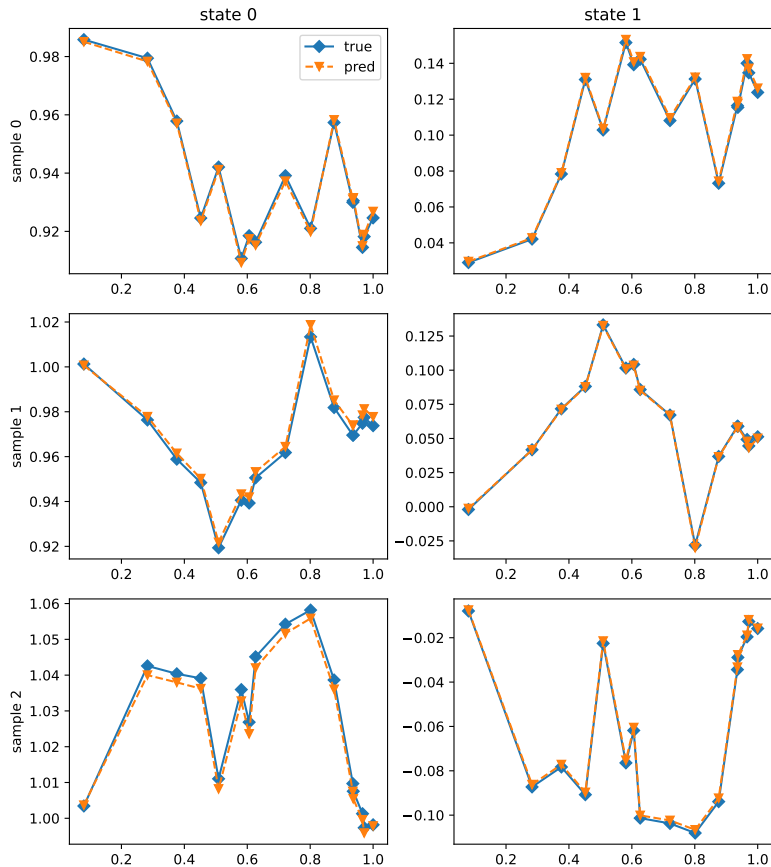


Figure 15: **Prediction of a linear system driven by Brownian motion using a model trained with only increments (level 1) data.** Three examples are taken from the test set with 16 intervals.

repeat the experiment over five random seeds. Like the sinusoid task, the training objective is the masked mean squared error over non-padded intervals.

Figure 5 and Table 3 report the test MSE as a function of the number of query intervals. Example output paths can be seen in Figures 15 and 16. As expected, the level-2 model achieves substantially lower error, especially when the number of query intervals is small. As the number of intervals increases, the gap between the two models decreases. When the partition is refined, each interval becomes shorter, and the effect of unobserved second-level terms on each interval becomes smaller. The level-1 model can therefore partially compensate for the lack of second level information by using more frequent updates. However, the level-2 model remains more accurate across the interval counts considered, confirming that our approach can incorporate and exploit higher-order information directly when such information is available.

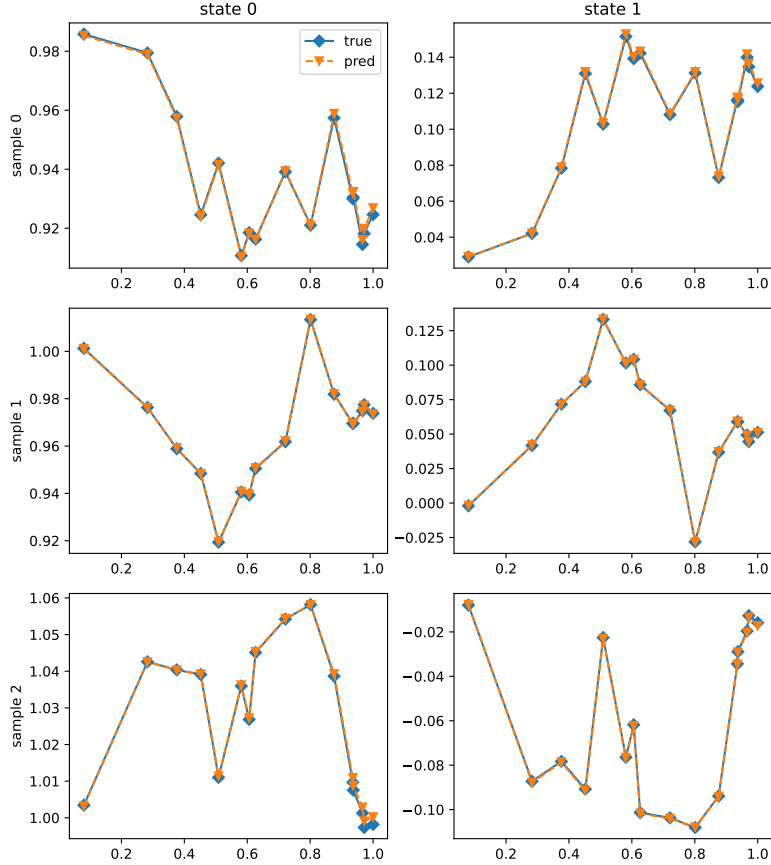


Figure 16: **Prediction of a linear system driven by Brownian motion using a model trained with both increments and area (level 2) data.** Three examples are taken from the test set with 16 intervals.

### C.3 UEA experiments

We follow the UEA multivariate time series classification archive (UEA-MTSCA) [Bagnall et al., 2018] protocol of Walker et al. [2024] and the SLiCE protocol of Walker et al. [2025]. The benchmark consists of EigenWorms, EthanolConcentration, Heartbeat, MotorImagery, SelfRegulationSCP1, and SelfRegulationSCP2. As in Walker et al. [2024], duplicated EigenWorms series are removed before splitting. The original train and test cases are pooled and re-split into train, validation, and test sets with relative sizes 70/15/15. Hyperparameters are selected using validation accuracy on a fixed random split and are then kept fixed for evaluation over five random seeds.

The recurrent baselines are S5, LRU, S6, and Mamba [Smith et al., 2023, Orvieto et al., 2023, Gu and Dao, 2024]. The continuous baselines are an NCDE with Hermite cubic interpolation and backward differences [Kidger et al., 2020], and a Log-NCDE, diagonal SLiCE (D-SLiCE), and block-diagonal SLiCE (BD-SLiCE) using our embedding [Walker et al., 2024, 2025]. The aim of these experiments is not to establish a new state of the art on the UEA-MTSCA benchmark. The selected baselines are chosen to match the protocols of Walker et al. [2024] and Walker et al. [2025], and we keep the selected hyperparameters fixed rather than re-tuning each model for the dropped-input setting. Recent models, including Rough Transformers [Moreno-Pino et al., 2024], oscillatory state-space models such as LinOSS [Rusch and Rus, 2025] and D-LinOSS [Boyer et al., 2025], and nonlinear parallel state-space models such as LrcSSM [Farsang et al., 2025], report higher no-drop accuracies on this six-dataset benchmark. Our comparison instead focuses on the effect of the proposed embedding and interval-level Log-ODE computation under controlled hyperparameters and increasing input sparsification.

Since the task is classification, time is treated as a discretely observed variable when included in the driving path, and there are no continuously observed variables. For D-SLiCE and BD-SLiCE, we use the Log-NCDE hyperparameters selected by Walker et al. [2024], replacing only the non-linear vector field by the corresponding structured linear vector field, following Walker et al. [2025]. For BD-SLiCE, the block size is  $b_i = 4$ . For the

Table 4: **Log-NCDE hyperparameters for the UEA path models.** D-SLiCE and BD-SLiCE use the same settings as Log-NCDE, replacing only the vector field structure.

Dataset	LR	Include time	Hidden Dimension	Log-ODE		$\lambda$
				Depth	Step	
EW	$10^{-3}$	✓	128	2	12	$10^{-3}$
EC	$10^{-4}$	✓	64	1	1	$10^{-6}$
HB	$10^{-3}$	✓	16	2	2	$10^{-6}$
MI	$10^{-3}$	×	16	2	16	$10^{-3}$
SCP1	$10^{-4}$	×	64	2	16	0
SCP2	$10^{-4}$	×	128	2	4	$10^{-3}$

Table 5: **Selected recurrent-model hyperparameters for the UEA experiments.** The values are those selected by the hyperparameter optimisation of Walker et al. [2024] and are kept fixed in all dropping experiments.

Model	Hyperparameter	EW	EC	HB	MI	SCP1	SCP2
LRU	LR	$10^{-3}$	$10^{-5}$	$10^{-4}$	$10^{-3}$	$10^{-3}$	$10^{-3}$
	Include time	×	✓	✓	×	×	✓
	Hidden dimension	64	64	128	16	64	64
	Layers	4	6	2	6	2	2
	State dimension	64	16	256	256	16	16
S5	LR	$10^{-4}$	$10^{-5}$	$10^{-3}$	$10^{-3}$	$10^{-3}$	$10^{-4}$
	Include time	✓	✓	×	×	×	✓
	Hidden dimension	64	128	128	16	128	16
	Layers	2	2	4	6	6	2
	State dimension	16	16	16	64	16	64
	Init. blocks	8	8	4	4	8	2
S6	LR	$10^{-3}$	$10^{-5}$	$10^{-3}$	$10^{-3}$	$10^{-4}$	$10^{-3}$
	Include time	×	✓	✓	✓	×	×
	Hidden dimension	16	16	16	16	64	16
	Layers	4	4	4	4	2	2
	State dimension	64	16	16	256	16	256
Mamba	LR	$10^{-3}$	$10^{-3}$	$10^{-4}$	$10^{-5}$	$10^{-5}$	$10^{-4}$
	Include time	✓	✓	×	×	×	✓
	Hidden dimension	16	64	64	128	128	64
	Layers	6	4	4	2	2	6
	State dimension	64	256	256	64	16	64
	Conv. dimension	2	4	2	3	4	2
Expansion factor	1	4	4	1	1	2	

SLiCE models with the Log-ODE method, flows are composed using an associative parallel scan with chunks of size 128. Table 4 gives the Log-NCDE hyperparameters used by Log-NCDE, D-SLiCE, and BD-SLiCE. Table 5 gives the selected hyperparameters for the recurrent baselines. All of these hyperparameters are kept fixed across the no-drop and input-dropping experiments.

All reported accuracies are test accuracies in percent, reported as mean  $\pm$  standard deviation over five seeds. Average accuracy is the macro-average over the six datasets. Average rank is computed by ranking the models separately on each dataset at a fixed dropping level and averaging the ranks over datasets. No-drop values marked with  $\dagger$  are taken from Walker et al. [2024], and no-drop values marked with  $\ddagger$  are taken from Walker et al. [2025]. All dropped-input results are produced by our runs using the same selected hyperparameters, without retuning for the drop level.

### C.3.1 EigenWorms

EigenWorms is additionally used for the timing and memory comparison in Table 1 because it is the longest UEA dataset in the benchmark, with 17,984 observations per series. This makes it a direct stress test of whether the Log-ODE method can reduce the cost of long input streams. For this experiment, we keep the hyperparameters fixed to the values selected in the UEA protocol above and compare each model family with and without interval-level Log-ODE updates.

Table 6: **Per-dataset test accuracy (mean  $\pm$  std over 5 seeds, in %) for the UEA benchmark at no drop, with macro-average accuracy and average dataset rank.** Lower rank is better.

Model	EigenWorms	Ethanol	Heartbeat	MotorImagery	SCP1	SCP2	Avg. Acc.	Avg. Rank
S5	81.1 $\pm$ 3.7	24.1 $\pm$ 4.3	<u>77.7 <math>\pm</math> 5.5</u>	47.7 $\pm$ 5.5	<b>89.9 <math>\pm</math> 4.6</b>	50.5 $\pm$ 2.6	61.8	4.67
LRU	<b>87.8 <math>\pm</math> 2.8</b>	21.5 $\pm$ 2.1	<b>78.4 <math>\pm</math> 6.7</b>	48.4 $\pm$ 5.0	82.6 $\pm$ 3.4	51.2 $\pm$ 3.6	61.7	4.50
S6	85.0 $\pm$ 16.1	26.4 $\pm$ 6.4	76.5 $\pm$ 8.3	51.3 $\pm$ 4.7	82.8 $\pm$ 2.7	49.8 $\pm$ 9.5	62.0	5.00
Mamba	70.9 $\pm$ 15.8	27.9 $\pm$ 4.5	76.2 $\pm$ 3.8	47.7 $\pm$ 4.5	80.7 $\pm$ 1.4	48.2 $\pm$ 3.9	58.6	6.67
NCDE	75.0 $\pm$ 3.9	29.9 $\pm$ 6.5	73.9 $\pm$ 2.6	49.5 $\pm$ 2.8	79.8 $\pm$ 5.6	53.0 $\pm$ 2.8	60.2	5.33
Log-NCDE	85.6 $\pm$ 5.1	<b>34.4 <math>\pm</math> 6.4</b>	75.2 $\pm$ 4.6	<u>53.7 <math>\pm</math> 5.3</u>	83.1 $\pm$ 2.8	<u>53.7 <math>\pm</math> 4.1</u>	<b>64.3</b>	<u>3.00</u>
D-SLiCE	79.4 $\pm$ 5.7	27.1 $\pm$ 4.6	72.9 $\pm$ 5.0	<b>54.4 <math>\pm</math> 6.3</b>	83.5 $\pm$ 2.1	53.0 $\pm$ 5.8	61.7	4.50
BD-SLiCE	<u>86.1 <math>\pm</math> 3.5</u>	28.6 $\pm$ 6.4	77.4 $\pm$ 5.6	53.0 $\pm$ 2.0	<u>84.9 <math>\pm</math> 1.9</u>	<b>54.0 <math>\pm</math> 7.4</b>	<u>64.0</u>	<b>2.33</b>

Table 7: **Per-dataset test accuracy (mean  $\pm$  std over 5 seeds, in %) for the UEA benchmark at 30% drop, with macro-average accuracy and average dataset rank.** Lower rank is better.

Model	EigenWorms	Ethanol	Heartbeat	MotorImagery	SCP1	SCP2	Avg. Acc.	Avg. Rank
S5	79.4 $\pm$ 4.2	26.6 $\pm$ 1.1	<u>74.8 <math>\pm</math> 2.4</u>	<b>58.9 <math>\pm</math> 2.9</b>	<b>88.7 <math>\pm</math> 1.6</b>	51.9 $\pm$ 4.4	63.4	3.25
LRU	78.9 $\pm$ 6.2	25.3 $\pm$ 4.7	70.3 $\pm$ 4.6	56.8 $\pm$ 5.6	82.6 $\pm$ 3.1	51.2 $\pm$ 1.7	60.9	5.58
S6	80.0 $\pm$ 10.5	25.9 $\pm$ 6.7	74.0 $\pm$ 7.5	42.4 $\pm$ 4.0	78.0 $\pm$ 5.2	50.1 $\pm$ 8.4	58.4	6.50
Mamba	65.3 $\pm$ 15.8	27.2 $\pm$ 1.8	74.8 $\pm$ 6.2	51.3 $\pm$ 2.5	80.4 $\pm$ 1.9	<b>57.7 <math>\pm</math> 4.6</b>	59.5	4.83
NCDE	77.8 $\pm$ 4.6	28.9 $\pm$ 7.0	67.1 $\pm$ 4.3	51.2 $\pm$ 5.6	80.5 $\pm$ 6.5	51.9 $\pm$ 3.8	59.6	5.92
Log-NCDE	<u>82.8 <math>\pm</math> 7.3</u>	<b>37.2 <math>\pm</math> 3.6</b>	74.2 $\pm$ 4.6	54.7 $\pm$ 6.2	82.6 $\pm$ 2.2	53.7 $\pm$ 6.7	<b>64.2</b>	<u>3.08</u>
D-SLiCE	<u>76.7 <math>\pm</math> 5.4</u>	27.3 $\pm$ 4.8	<b>77.4 <math>\pm</math> 6.5</b>	51.2 $\pm$ 3.9	84.0 $\pm$ 1.8	<u>53.7 <math>\pm</math> 5.3</u>	61.7	3.83
BD-SLiCE	<b>84.4 <math>\pm</math> 4.2</b>	<u>32.7 <math>\pm</math> 4.6</u>	69.0 $\pm$ 10.0	<u>57.9 <math>\pm</math> 3.1</u>	<u>85.4 <math>\pm</math> 2.8</u>	53.0 $\pm$ 3.4	<u>63.7</u>	<b>3.00</b>

For the nonlinear NCDE family, the non-Log-ODE row corresponds to the standard NCDE baseline and the Log-ODE row corresponds to the Log-NCDE. For the dense linear and block-diagonal linear families, all rows are computed in parallel-in-time using an associative scan. The non-Log-ODE rows use depth-1 Log-ODE updates on intervals aligned with consecutive observations. This is equivalent to solving the CDE exactly with a linearly interpolated observation path. The Log-ODE rows instead use the selected coarser interval partition and higher-order interval log-signatures, then compose the resulting linear flows with the same associative-scan mechanism. Thus the comparison isolates the effect of replacing observation-level updates by interval-level Log-ODE updates, while keeping the architecture family and selected hyperparameters fixed.

Timing and memory are measured on an NVIDIA H100 GPU with batch size 1. The reported time is the wall-clock time per training step averaged over 1000 training steps and the reported memory is peak GPU memory. The EigenWorms results show that the Log-ODE method is beneficial for all three model families. In particular, BD-SLiCE with Log-ODE achieves higher accuracy than the standard NCDE baseline while reducing the time per training step from 26.02 seconds to 0.009 seconds.

### C.3.2 Input dropping

The input-dropping experiments test robustness to sparsification of the observed stream. For each drop level  $p \in \{0.3, 0.7, 0.95\}$ , a random mask is sampled independently for each series and applied to the input before model-specific preprocessing. All models use the same hyperparameters as in the no-drop setting, with no retuning for the drop level. The same drop level is used throughout each run, and results are averaged over five seeds.

For path-based models, dropping observations changes the observed stream but should not change the physical time horizon. We therefore keep the original Log-ODE query partition from the undropped series fixed, and recompute each interval log-signature using the surviving observations whose timestamps fall in that interval. If no discrete observation remains in an interval, the interval still contributes time, if it is included as a channel in the path. This preserves the original temporal alignment and avoids shortening or rescaling the path after observations are removed.

For the discrete recurrent models S5, LRU, S6, and Mamba, the randomly retained observations are passed directly to the model in chronological order. When the selected hyperparameters include time, the timestamp is retained as an input channel after dropping. When time is not included, the model receives only the retained observed values.

Table 2 summarises the results across the six datasets. Tables 6–9 give the corresponding per-dataset results. The continuous-time models using our embedding remain competitive across all drop levels. BD-SLiCE is the most stable model under severe sparsification, with its macro-average accuracy changing from 64.0% with no dropping to 62.5% with 95% dropping.

Table 8: **Per-dataset test accuracy (mean  $\pm$  std over 5 seeds, in %) for the UEA benchmark at 70% drop, with macro-average accuracy and average dataset rank.** Lower rank is better.

Model	EigenWorms	Ethanol	Heartbeat	MotorImagery	SCP1	SCP2	Avg. Acc.	Avg. Rank
S5	72.8 $\pm$ 3.2	27.3 $\pm$ 1.3	70.3 $\pm$ 4.3	<b>56.5 <math>\pm</math> 6.4</b>	<u>85.4 <math>\pm</math> 2.2</u>	48.4 $\pm$ 6.2	60.1	4.83
LRU	81.1 $\pm$ 6.4	25.3 $\pm$ 4.7	75.5 $\pm$ 6.6	54.4 $\pm$ 4.6	78.4 $\pm$ 3.8	51.2 $\pm$ 5.9	61.0	5.00
S6	84.7 $\pm$ 6.3	25.3 $\pm$ 7.4	76.1 $\pm$ 4.1	<u>51.3 <math>\pm</math> 2.2</u>	79.2 $\pm$ 1.9	51.7 $\pm$ 3.0	61.4	4.00
Mamba	<u>69.1 <math>\pm</math> 13.3</u>	27.2 $\pm$ 1.8	<b>76.7 <math>\pm</math> 5.8</b>	53.0 $\pm$ 2.2	79.2 $\pm$ 4.8	<b>58.4 <math>\pm</math> 3.2</b>	60.6	4.00
NCDE	78.9 $\pm$ 2.8	24.1 $\pm$ 6.2	69.7 $\pm$ 5.9	50.5 $\pm$ 2.3	80.2 $\pm$ 5.8	49.8 $\pm$ 5.9	58.9	6.42
Log-NCDE	<b>87.2 <math>\pm</math> 5.4</b>	<b>36.2 <math>\pm</math> 5.9</b>	73.5 $\pm$ 4.4	50.2 $\pm$ 5.5	78.8 $\pm$ 7.1	50.5 $\pm$ 7.6	<b>62.7</b>	4.67
D-SLiCE	80.6 $\pm$ 7.2	29.4 $\pm$ 8.2	<u>76.5 <math>\pm</math> 5.3</u>	50.2 $\pm$ 4.1	84.5 $\pm$ 3.7	51.9 $\pm$ 2.4	62.2	<u>3.83</u>
BD-SLiCE	81.7 $\pm$ 6.2	<u>31.9 <math>\pm</math> 5.1</u>	<u>72.6 <math>\pm</math> 5.8</u>	50.5 $\pm$ 3.2	<b>85.9 <math>\pm</math> 3.0</b>	<u>52.3 <math>\pm</math> 5.0</u>	<u>62.5</u>	<b>3.25</b>

Table 9: **Per-dataset test accuracy (mean  $\pm$  std over 5 seeds, in %) for the UEA benchmark at 95% drop, with macro-average accuracy and average dataset rank.** Lower rank is better.

Model	EigenWorms	Ethanol	Heartbeat	MotorImagery	SCP1	SCP2	Avg. Acc.	Avg. Rank
S5	61.1 $\pm$ 3.5	27.3 $\pm$ 1.3	70.3 $\pm$ 6.3	<b>53.7 <math>\pm</math> 5.7</b>	81.9 $\pm$ 4.4	45.6 $\pm$ 6.1	56.7	5.33
LRU	<b>83.9 <math>\pm</math> 2.7</b>	25.1 $\pm$ 4.8	71.6 $\pm$ 4.6	46.7 $\pm$ 6.5	81.6 $\pm$ 4.5	<b>56.1 <math>\pm</math> 8.4</b>	60.8	<u>4.17</u>
S6	78.8 $\pm$ 9.7	25.7 $\pm$ 6.9	71.5 $\pm$ 4.1	50.9 $\pm$ 4.2	74.9 $\pm$ 3.7	51.7 $\pm$ 3.2	58.9	5.17
Mamba	72.2 $\pm$ 12.2	27.2 $\pm$ 1.8	71.0 $\pm$ 8.2	46.6 $\pm$ 5.0	78.0 $\pm$ 1.8	50.5 $\pm$ 5.0	57.6	6.17
NCDE	77.2 $\pm$ 8.3	28.1 $\pm$ 2.5	68.7 $\pm$ 4.3	50.2 $\pm$ 5.2	76.9 $\pm$ 6.6	50.9 $\pm$ 3.5	58.7	5.33
Log-NCDE	81.7 $\pm$ 3.8	<b>34.9 <math>\pm</math> 4.7</b>	73.5 $\pm$ 6.8	49.8 $\pm$ 4.5	76.0 $\pm$ 4.7	49.5 $\pm$ 5.7	60.9	<u>4.17</u>
D-SLiCE	80.6 $\pm$ 5.3	30.6 $\pm$ 7.1	<b>75.2 <math>\pm</math> 4.8</b>	49.1 $\pm$ 4.6	84.5 $\pm$ 2.6	53.0 $\pm$ 3.6	<u>62.2</u>	<b>2.83</b>
BD-SLiCE	<u>83.3 <math>\pm</math> 3.5</u>	30.1 $\pm$ 9.3	<u>74.2 <math>\pm</math> 7.8</u>	<u>53.0 <math>\pm</math> 1.7</u>	<b>85.2 <math>\pm</math> 2.6</b>	49.5 $\pm$ 5.1	<b>62.5</b>	<b>2.83</b>